PAPER

Dye degradation performance, bactericidal behavior and molecular docking analysis of Cu-doped TiO₂ nanoparticles

M. Ikram, †*[a] E. Umar,†[c] A. Raza,[c] A. Haider,[b] S. Naz,[d] A. Ul-Hamid,[f] J. Haider,[d] I. Shahzadi,[e] J. Hassan[c] and S. Ali[c]

Copper-doped TiO₂ was prepared with a sol–gel chemical method. Various concentrations (3, 6, and 9 wt%) of Cu dopant were employed. Several techniques were implemented to assess the structural, optical, morphological and chemical properties of the synthesized samples. Evaluation of elemental composition using SEM-EDS and XRF techniques showed the presence of dopant element in the prepared samples. XRD analysis confirmed the presence of anatase (TiO₂) phase with interstitial doping. Incorporation of dopant was observed to enhance the crystallinity and increase the crystallite size of the synthesized products. SAED profiles revealed a high degree of crystallinity in the prepared specimens, which was also evident in the XRD spectra. Optical properties studied using UV-vis spectroscopy depicted a shift of the maximum absorption to the visible region (redshift) that signified a reduction in the band gap energy of Cu-doped TiO₂ samples. Examination of morphological features with scanning and high-resolution transmission electron microscopes revealed the formation of spherical nanoparticles with a tendency to agglomerate with increasing dopant concentration. Molecular vibrations and the formation of Ti–O–Ti bonds were revealed through FTIR spectra. PL spectroscopy recorded the trapping efficiency and migration of charge carriers, which exhibited electron–hole recombination behavior. Doped nanostructures showed enhanced bactericidal performance and synergism against *S. aureus* and *E. coli*. In summary, Cu-doped TiO₂ nanostructures were observed to impede bacteria effectively, which is deemed beneficial in overcoming ailments caused by pathogens such as microbial etiologies. Furthermore, molecular docking analysis was conducted to study the interaction of Cu-doped TiO₂ nanoparticles with multiple proteins namely β-lactamase (binding score: −4.91 kcal mol⁻¹), ddlB (binding score: −5.67 kcal mol⁻¹) and FabI (binding score: −6.13 kcal mol⁻¹) as possible targets with active site residues. Dye degradation/reduction of control and Cu-doped samples were studied through absorption spectroscopy. The obtained outcomes of the performed experiment indicated that the photocatalytic activity of Cu-TiO₂ enhanced with increasing dopant concentration, which is thought to be due to a decreased rate of electron–hole pair recombination. Consequently, it is suggested that Cu-TiO₂ can be exploited as an effective candidate for antibacterial and dye degradation applications.

[a]*Solar Cell Applications Research Lab, Department of Physics, Government College University Lahore, Punjab, 54000, Pakistan. E-mail: dr.muhammadikram@gcu.edu. pk; Tel: +923005406667*

[b]*Department of Clinical Medicine and Surgery, University of Veterinary and Animal Sciences, Lahore 54000, Punjab, Pakistan*

[c]*Department of Physics, Riphah Institute of Computing and Applied Sciences (RICAS), Riphah International University, 14 Ali Road, Lahore, Pakistan*

[d]*Tianjin Institute of Industrial Biotechnology, Chinese Academy of Sciences, Tianjin 300308, China*

[e]*College of Pharmacy, University of the Punjab, Lahore, 54000, Pakistan*

[f]*Center for Engineering Research, Research Institute, King Fahd University of Petroleum & Minerals, Dhahran, 31261, Saudi Arabia*

† M. Ikram and E. Umar are equal contributors.

1 Introduction

An increase in the world's population and rapid industrialization during the last century have contributed to environmental pollution, thus adversely affecting the quality of air and water that are deemed crucial for continued sustenance of life on earth. It is no wonder then that a lot of effort is currently being expended into finding effective means of reducing environmental pollutants to provide global citizens with a clean and wholesome ecosystem.[1–4] In this regard, study of photocatalytic materials has attracted significant attention over the last two decades with a large number of articles published on an annual basis. Concurrently, there has been substantial advancement in technology that is used to produce efficient and cost-effective photocatalysts. An increase in the efficiency of photocatalytic

materials synthesized nowadays has primarily been attributed to the advancement in nanotechnology.[2,5,6] Titanium dioxide (TiO$_2$) is considered to be one of the most remarkable photocatalysts due to its broad spectrum of applications, and its substantial stability and non-toxicity. TiO$_2$ has been employed in various applications as a photocatalyst, antimicrobial agent, and a solution to environmental problems, owing to its environment-friendly nature and cost-effectiveness. TiO$_2$ naturally exists in three crystallographic forms namely anatase, rutile, and brookite. Anatase phase is the most promising candidate for photocatalytic activity, particularly nanoparticles of anatase that are less than 14 nm in size are considered to be an ideal contender for use in wastewater treatment owing to their large surface area.[2,5,7–9]

In addition to the favorable characteristics mentioned above, it has been possible to improve upon the properties of TiO$_2$ through various modifications. As a consequence of these alterations, TiO$_2$ displays absorption in the visible region and in many cases photocatalytic activity under visible irradiation for various reactions.[2,7,10] The photocatalytic mechanism of titania is constrained by the tendency for electron–hole pairs to recombine, as is the case for all semiconductor photocatalysts. As a result of recombination of electron–holes, titania exhibits poor band gap emission, which optically allows for the irradiative recombination of trap states.[10–13] In general, recombination instigated by impurities and defects as well as various other aspects lead to incorporation of bulk and surface imperfections into crystals, which may occur either on the surface or in bulk. Additionally, decrease in particle size usually leads to an increase in surface recombination.[10,12,14] Addition of any species that expedite charge separation serves to reduce recombination phenomenon in the material and enhances overall quantum efficiency of the photocatalytic system. Charge separation in titania supported through various modifiers such as noble metals, heterojunction coupling, and doping with transition metal ions has been reported.[10,12,15,16]

Taking into account the limitations listed above, copper incorporated in various concentrations in pure TiO$_2$ stands out as one of the most favorable dopant materials that compensates for such drawbacks.[17,18] The Cu-based nanocatalysts have significant applications in nanotechnology including photocatalysis, electrolysis, hydrogen production, and anti-bacterial products. Previously reported literature has revealed that high concentrations of Cu have been utilized to enhance photocatalytic and anti-bacterial efficiency.[10,17,19] In comparison with noble metals (*i.e.*, Au, Pd, and Ag), Cu has been considered as a highly competent co-catalyst of titania due to its ease of availability, and cost-effectiveness in that it is 100 and 6000 times cheaper than Ag and gold, respectively.[10,13,20,21] The photoenhancement of Cu compared to other dopants was determined in the following order: Cu-TiO$_2$ > Au-TiO$_2$ > Ag-TiO$_2$ > TiO$_2$.[22] It is considered favorable to dope Cu ions in pristine TiO$_2$ crystal lattice since ionic radius of Cu^{2+} is 0.087 nm, which is slightly larger than Ti^{4+} radius of 0.074 nm. In addition, a large difference in their valence states indicates that Cu^{2+} could not replace Ti^{4+} at its location within the crystal lattice for substitutional doping to take place. Therefore, the only possibility is the incorporation of Cu^{2+} ions at the interstitial sites of the crystal lattice.[10,23]

Apart from the afore discussed applications of TiO$_2$, the next promising application of TiO$_2$ nanoparticles is as an antimicrobial agent. The antimicrobial activity of TiO$_2$ nanoparticles is attributed to oxidative stress present due to the generation of reactive oxygen species (ROS) containing hydroxyl radicals (*e.g.* OH$^\cdot$) and production of hydrogen peroxide (*e.g.* H$_2$O$_2$) under ultra-visible light. Consequently, TiO$_2$ can be used as a potential antibacterial agent.[24–26] The produced ROS leads to a direct contact between cells and nanoparticles, which causes cell death due to the damage induced in the cell membrane and DNA, ultimately resulting in cessation of cell cycle.[7,24,27] It prevents and destroys major pathogens and foodborne bacteria such as *E. coli*, methicillin-resistant *Staphylococcus aureus* (MRSA), *Bacillus subtilis*, *S. aureus*, and *Pseudomonas*. The high level of antimicrobial activity ascribed to Cu dopant in various studies is directly associated with the release of ions that causes oxidative stress with the production of ROS under aerobic circumstances.[27–29] The ions are released due to the penetration of Cu into the cell after the membrane is degraded while an increase in the volume of intrinsic Cu induces significant oxidative stress as revealed by redox cycling among various forms of Cu *i.e.*, native Cu, Cu(I), and Cu(II).[29–31] In the current research work, we aimed to synthesize TiO$_2$ nanoparticles doped with various concentrations (3, 6, and 9 wt%) of Cu through sol–gel method. The prepared samples were characterized by using various techniques such as XRD, FTIR, UV-vis, PL, FESEM & HR-TEM. The synthesized products were employed as photocatalysts to treat industrial wastewater and remove synthetic dye (Methylene blue). Furthermore, the level of its antimicrobial activity was tested against methicillin-resistant *Staphylococcus aureus* (MRSA). The high antibacterial activity of Cu-doped TiO$_2$ against *S. aureus* was attributed to cell wall rupture and/or to other biosynthetic pathways considered vital for bacterial survival and growth. Molecular docking analysis was conducted to provide an insight into the interaction pattern of Cu-doped TiO$_2$ nanoparticles with selected protein targets such as β-lactamase, ddlB and FabI that belong to peptidoglycan and fatty acids biosynthetic pathways, respectively.

2 Experimental methods

2.1 Chemicals

Titanium(IV) butoxide (C$_{16}$H$_{36}$O$_4$Ti) and copper acetate (Cu(CH$_3$COO)$_2$) were obtained from "Sigma-Aldrich". Hydrochloric acid (HCl, 37%), methanol (CH$_3$OH) and ethanol (C$_2$H$_5$OH) were acquired from "Analar".

2.2 Synthesis of bare and Cu-doped TiO$_2$

Pristine and Cu-doped TiO$_2$ nanoparticles were synthesized through sol–gel route, using 10 ml titanium(IV) butoxide with 50 ml methanol, 3 ml deionized water (DIW) and 2 ml HCl. The mixture was stirred for 15 minutes (solution A). Various concentrations of copper acetate (3, 6, 9 wt%) were vigorously

dissolved in DIW (solution B). Subsequently, solution B was added dropwise into solution A under constant stirring. During synthesis, mixture of water and ethanol was added gradually and solution was magnetically stirred at 50 °C for 2 hours. Finally, prepared products were annealed at 400 °C to acquire nanoparticles of anatase as shown in Fig. 1.[32]

2.3 Evaluation of photocatalytic activity

The photocatalytic activity of the prepared products was evaluated by assessing degradation rate of certain industrial pollutants such as synthetic and toxic methylene blue (MB) dye in aqueous solution as displayed in Fig. 2. The stock solution of MB (1 g/1 ml) was prepared and 10 mg of prepared sample (pure TiO_2, 0.03 : 1, 0.06 : 1, 0.09 : 1) was mixed with 60 ml stock solution which was then placed in dark for 30 minutes to achieve significant equilibrium between MB and photocatalyst prior to illumination. After vigorous stirring for 15 minutes, the solution was reassigned to a photoreactor operated with Hg lamp (400 W with a wavelength of 400–700 nm) as a visible light source. A distance of 15 cm was kept between the solution and light source to prevent overheating. After complete exposure of light for a fixed time interval of 20 minutes, 3 ml of solution was extracted to measure dye concentration using UV-vis spectrograph at $\lambda_{max} = 665$ nm of MB absorbance. Dye absorbance decreased gradually at λ_{max} after ordered time intervals that demonstrated decolorization rate and PCA efficiency of photocatalysts.

$$\text{Degradation efficiency (\%)} = \left[\frac{C_o - C}{C_o}\right] \times 100 \qquad (a)$$

where C_o corresponds to initial absorbance (i.e. $t = 0$) and C refers to final absorbance at time t.[12,33] The collected solution

was centrifuged at 4000 rpm for 5 minutes to remove photocatalyst from the solution.

2.3.1 Reaction mechanism and kinetics. Reaction mechanism involved in photocatalytic experimentation to assess dye degradation of organic molecules can be described as (see Fig. 2).

(a) Photoexcitation. The photocatalytic reaction is instigated by photons with energy ($E = h\nu$) equal to or greater than the band gap energy while photoelectrons (e^-) are shifted from the lower/valance (VB) to higher/conduction band (CB). The excitation process generates a hole in VB thus resulting in one electron–hole pair (e^-–h^+) as depicted in eqn (1)

$$TiO_2 + h\nu \rightarrow TiO_2(e^-) + h^+ \qquad (1)$$
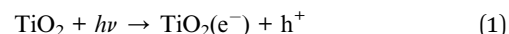
(b) Ionization of water. Photogenerated h^+ produce OH· free radical upon reaction with water:

$$H_2O(ads) + h^+ \rightarrow OH^·(ads) + H^+(ads) \qquad (2)$$

The HO· radical produced on the irradiated surface of semiconductor is a strong oxidant agent. It selectively targets adsorbed organic molecules or those which are very close to the catalyst surface, which contributes to mineralization depending on the structure and degree of stability. Not only it can quickly target biological compounds, but microorganisms can be killed to enhance decontamination.

(c) Oxygen ionosorption. Photogenerated electrons bind with the surface-bonded water molecules (OH^-) to generate hydroxyl radicals while electrons are readily trapped by oxygen molecules to produce superoxide radicals (O_2^-).
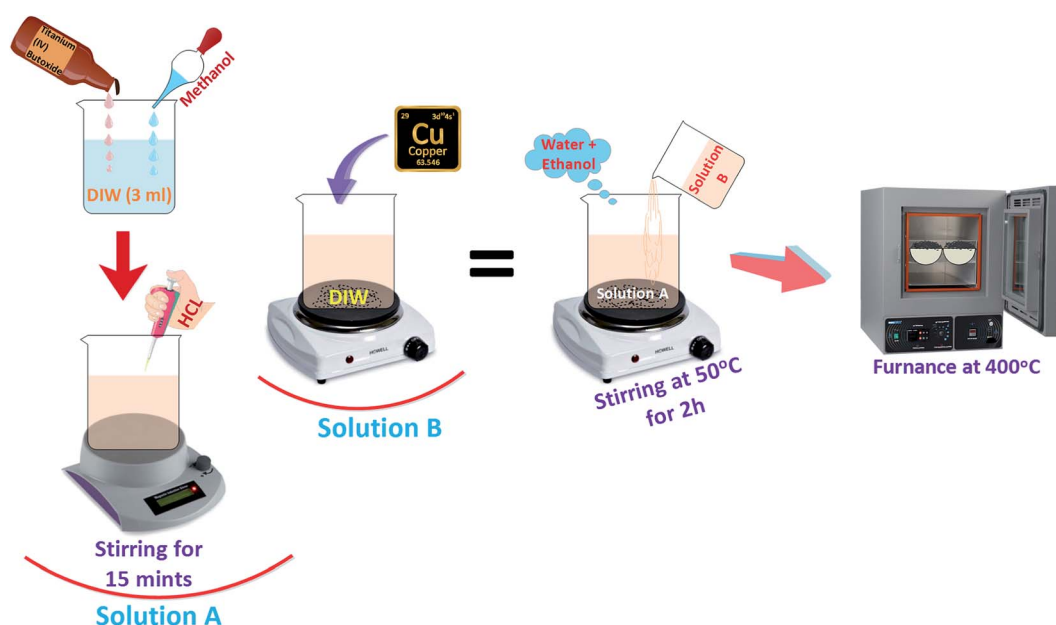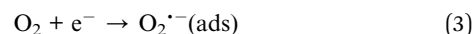
$$O_2 + e^- \rightarrow O_2^{·-}(ads) \qquad (3)$$

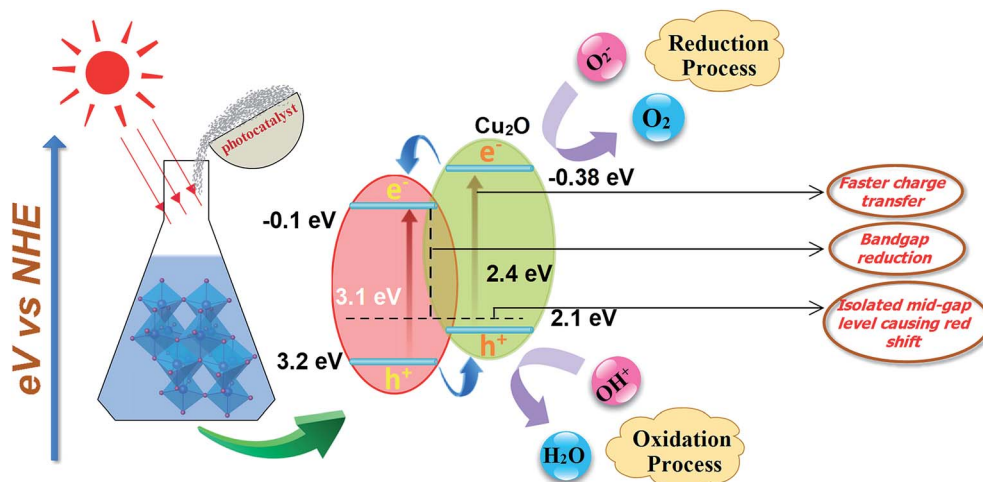**Fig. 1** Synthesis process for TiO_2 and Cu-doped TiO_2 nanoparticles.

Fig. 2 Photocatalytic mechanism of dye degradation in the presence of Cu-TiO$_2$ photocatalyst.

The superoxide ion can not only take part in more oxidation cycles, but it can also inhibit recombination of e$^-$–h$^+$ and thus serves to keep TiO$_2$ molecule neutral.

(d) Protonation of superoxide. Superoxide ions (O$_2{}^-$) provide protonated hydroperoxylate radical (H$_2$O$^•$) and finally H$_2$O$_2$ is dissociated into strongly reactive OH$^•$. Generally, the degradation reaction of organic pollutants is believed to be initiated by the $^•$OH radical, which is formed through the oxidation of H$_2$O

by h$^+$ and can oxidize almost all organic compounds. O$_2$, the final oxidant of the whole photocatalytic oxidation process, is exclusively considered a scavenger of e$^-$, which serves to depress recombination of photogenerated h$^+$/e$^-$ pairs and regenerate photocatalyst.

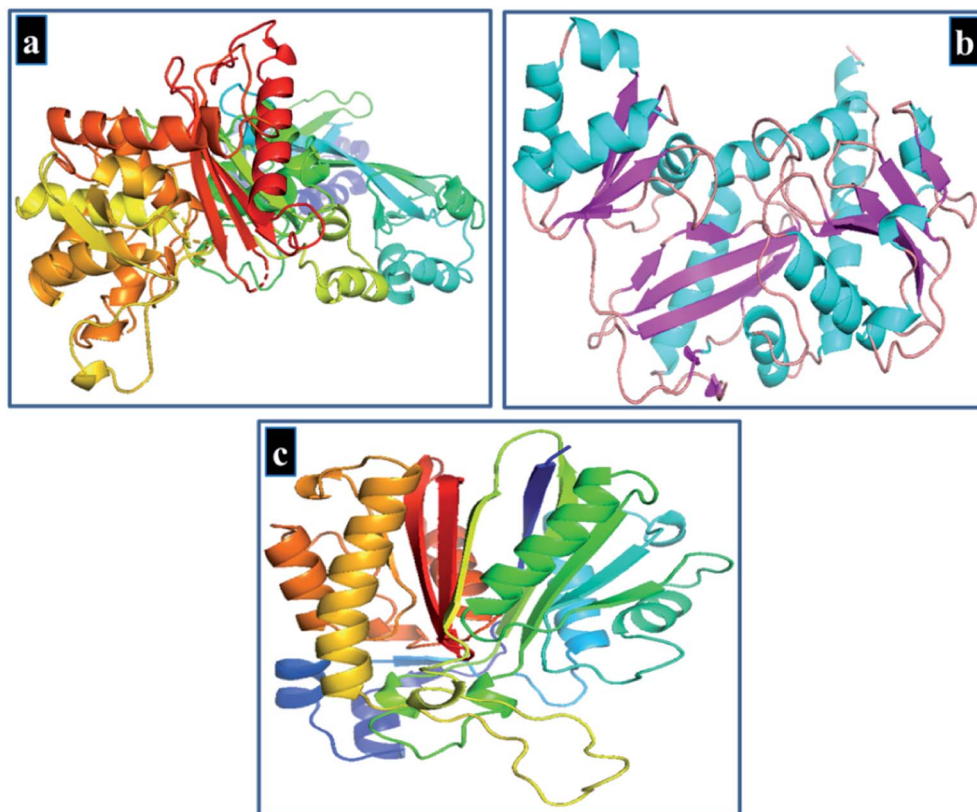$$O_2{}^{•-}(ads) + H^+ \rightleftharpoons HOO^•(ads) \qquad (4)$$

Fig. 3 3D-Structure of target proteins of *S. aureus*, (a) beta lactamase (PDB 1MWU), (b) ddlB (PDB 2I80), (c) FabI (PDB 4Z8D).
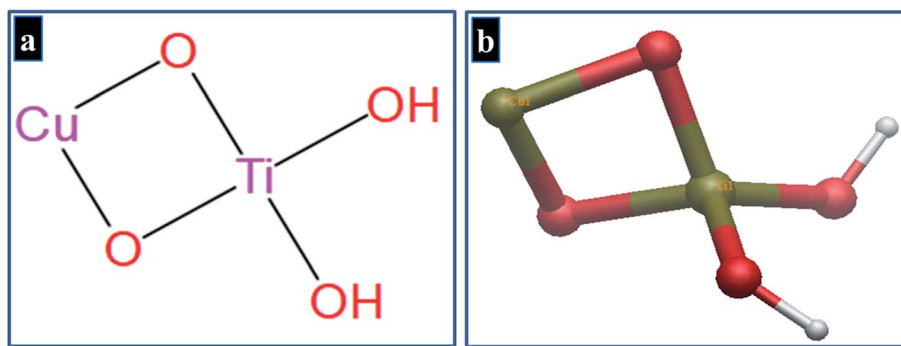
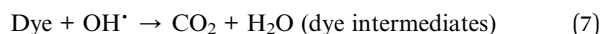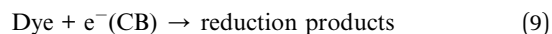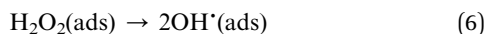**Fig. 4** Structure of Cu-doped TiO_2 nanoparticles in (a) 2D and (b) 3D view.

$$2HOO^\bullet(ads) \rightarrow H_2O_2(ads) + O_2 \quad (5)$$

$$H_2O_2(ads) \rightarrow 2OH^\bullet(ads) \quad (6)$$

$$Dye + OH^\bullet \rightarrow CO_2 + H_2O \text{ (dye intermediates)} \quad (7)$$

$$Dye + h^+(VB) \rightarrow \text{oxidation products} \quad (8)$$

$$Dye + e^-(CB) \rightarrow \text{reduction products} \quad (9)$$
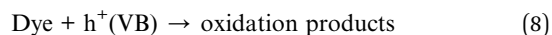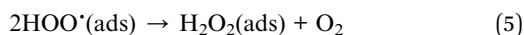
Oxidation and reduction processes take place simultaneously on the surface of photo-excited photocatalyst.[34,35]
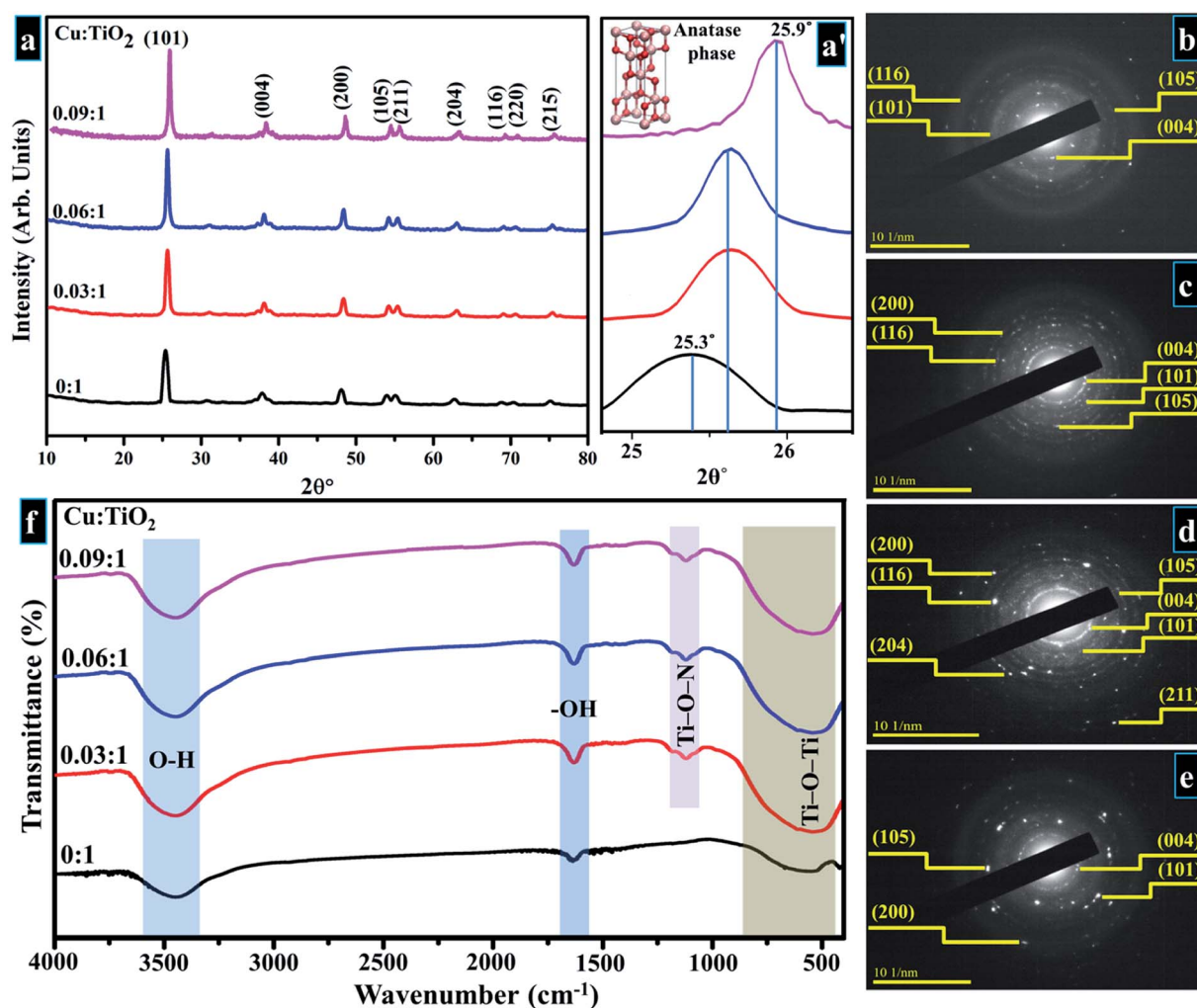

Fig. 5 (a) XRD pattern (a') zoomed area of (101) plane (b–e) SAED profiles of as-prepared and Cu-doped TiO_2 (b) 0 : 1 (c) 0.03 : 1 (d) 0.06 : 1 (e) 0.09 : 1 (f) FTIR spectra.

Table 1 Average crystallite size and E_g values with Cu concentration

Cu : TiO$_2$	Crystallite size (nm)	E_g (eV)
0 : 1	22.22	3.1
0.03 : 1	20.09	2.8
0.06 : 1	18.17	2.6
0.09 : 1	15.47	2.4

According to this mechanism, the trapping of e$^-$ by O$_2$ only determines the rate of the photocatalytic reaction, but not change the reaction pathway and mechanism. However, recent studies have indicated that the participation of O$_2$ in the photocatalytic reaction would greatly influence degradation product distribution. In the photocatalytic reaction, the h$^+$-induced oxidation half-reaction and e$^-$-induced reduction half-reaction proceed on the surface of one photocatalyst particle (usually of a nano-size) at the same time, which makes it difficult to distinguish them in space and time.[35]

2.4 Isolation and identification of *S. aureus* and *E. coli*

Sheep (ovine) milk samples designated positive for clinical mastitis were collected from private farms of Punjab (Pakistan) and cultured on 5% sheep blood agar (SBA). The cultured isolates were further purified by streaking on MacConkey Agar (MA) and mannitol salt agar (MSA) in triplets in order to isolate *E. coli* and *S. aureus*, respectively. Morphological and biochemical characterization of purified isolates was undertaken through Gram's staining, catalase, and coagulase tests.[36,37]

2.5 Antimicrobial activity

Antimicrobial evaluation of Cu-doped TiO$_2$ was conducted through agar well diffusion assay by swabbing 1.5×10^8 CFU ml^{-1} of isolated G −ve and G +ve stains on MA and MSA, respectively. Various concentrations of Cu-doped TiO$_2$ (0.5 and 1.0 mg/50 μl) was poured as low and high dose into 6 mm wells on MA and MSA plates formed with sterile cork borer with a micropipette. Ciprofloxacin (0.005 mg/50 μl) and distal water (50 μl) were employed as control positive (+ve) and negative (−ve), respectively. Antimicrobial efficacy was assessed by measuring inhibition zones (mm) using Vernier caliper after overnight incubation of Petri plates at 37 °C. The antimicrobial efficacy of Cu-doped TiO$_2$ was considered statistically significant using one-way analysis of variance (ANOVA).[38]

2.6 Molecular docking analysis

In silico or computational studies have attracted much attention in recent decades as it has enabled scientists to understand the behavior of biomolecules at atomic level. Keeping in view the high antibacterial activity exhibited by Cu-doped TiO$_2$ nanoparticles against *S. aureus*, their molecular docking analysis was performed against selected protein targets belonging to cell wall and fatty acids biosynthetic pathways that are vital for bacterial survival.[39] Molecular docking study was undertaken against two enzyme targets namely D-alanine-D-alanine ligase B (ddlB) and β-lactamase of cell wall biosynthetic pathway while enoyl-[acyl-carrier-protein] reductase (FabI) was selected as a possible target from fatty acid biosynthetic pathway.[40,41]

The crystal structure of target proteins were obtained from protein data bank with PDB ID 1MWU; resolution: 2.6 Å (ref. 42) and 2I80; resolution: 2.2 Å (ref. 43) for β-lactamase and D-alanine-D-alanine ligase B of *S. aureus*, respectively as shown in Fig. 3. In addition, PDB ID 4Z8D[44] was selected for enoyl-[acyl-carrier-protein] reductase (FabI) from *S. aureus*.

The ICM v3.8-4a or above (Molsoft L.L.C., La Jolla, CA) software was employed for molecular docking study[45] while protein structure was prepared using the receptor preparation tool of ICM Molsoft that involved removal of water molecules and co-
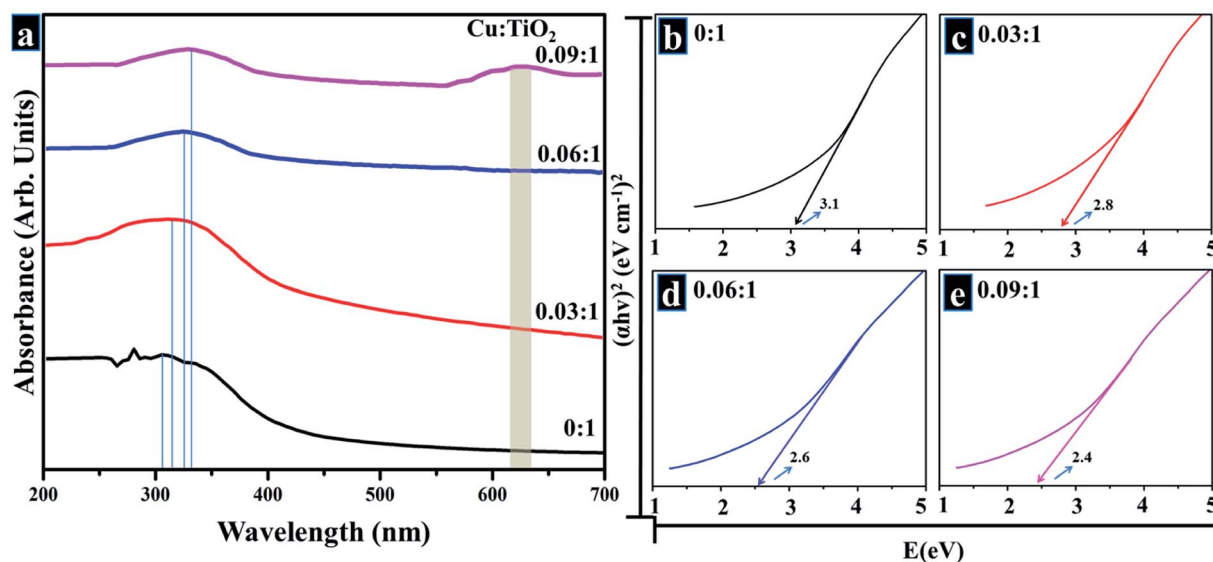

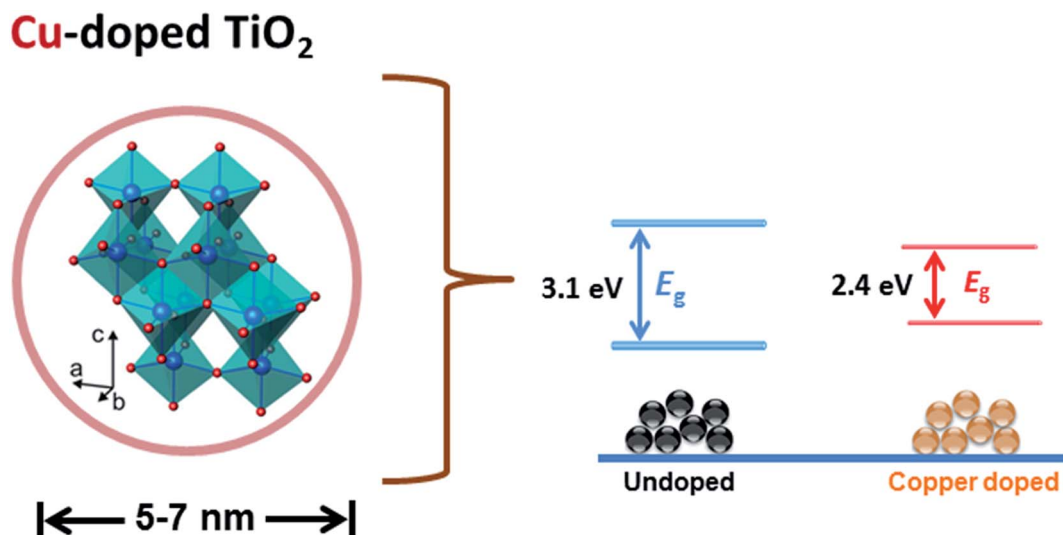**Fig. 6** (a) Optical absorbance spectra (b−e) band gap determination.

Fig. 7 Schematic representation of band gap energy reduction.

crystallized ligand. Protein structures were optimized using default parameters and binding pocket was specified using a grid box. The structure of Cu-doped TiO_2 nanoparticles was prepared by modifying crystal structure of anatase (TiO_2) retrieved from PubChem in.cif format using Gaussian 09 software and is shown in Fig. 4(a and b). Finally, 10 best-docked conformations were generated for each target protein to get an insight into interaction pattern of nanoparticles with active site residues.

The crystal structure of Cu-doped TiO_2 is composed of repeating unit cells in a regular array. The basic monomeric structure of Cu-doped TiO_2 is used as a representative of whole crystal structure to evaluate various possible interactions with active site residues.[46] The selected protein targets inside bacterial cell have natural environment of solvents, ions *etc.*, that need to be considered for *in silico* predictions. The NPs penetrate into active pocket as monomeric units and interact with various residues in the form of electrostatic, hydrophobic and van der Waals interactions. The whole crystal structure cannot be employed to represent a clear view of interaction pattern at atomistic level.

2.7 Materials characterization

Crystal structure and phase transition of Cu-TiO_2 were assessed through XRD using Spectrum Bruker system (XRD, D2 Phaser, USA) equipped with monochromatic Cu K-α ($\lambda = 0.154$ nm and $2\theta = 5$–$80°$) set at a scan rate of $0.05°$ min^{-1}. Chemical analysis and study of attached functional groups were undertaken using FTIR PerkinElmer 3100 spectrometer with a spectral range of 4000–500 cm^{-1} in 32 scans and a resolution of 0.2 cm^{-1}. Optical properties were analyzed through UV-vis spectrophotometer (Genesys 10S) ranging from 200 to 700 nm. Surface morphology and *d*-spacing of synthesized specimens were observed through FESEM coupled with EDS spectrometer, JSM-6460LV, and HR-TEM Philips CM30 and JEOL JEM 2100F. PL spectroscopy was carried out to study migration and recombination of electron–hole pairs using a spectrofluorometer (JASCO, FP-8300).

3 Results and discussion

Crystallographic plane structure, phase purity, and crystallite size of synthesized products were determined by means of XRD; obtained results are shown in Fig. 5a. In XRD spectra, well-defined peaks are sited at $\sim25.37°$, $37.79°$, $48.18°$, $53.87°$, $55.17°$, $62.68°$, $68.74°$, $70.29°$ and $75.05°$ which are allotted to (101), (004), (200), (105), (211), (204), (116), (220), and (215) facets, respectively. These planes belong to tetragonal anatase phase of Cu-doped TiO_2 that correlates with standard spectrum (JCPDS card 21-1272) along with space group $I4_1/amd$ (141) with corresponding cell dimensions of $a = 3.758$ Å and $c = 9.513$ Å.[47–57] The lattice spacing is ~0.35 nm for TiO_2 equivalent to (101) facet, also validated with HR-TEM observation (see Fig. 9). A slight shift to lower values in layer spacing (0.33 nm) upon Cu doping is attributed to a thorough distribution of dopant element between interlayers of host sample.[24,52,53]

Upon Cu doping, no distinct peak of dopant or formation of any crystal phase of dopant species was observed in the acquired XRD spectra. This observation does not necessarily indicate that Cu-based planes/phases are not present in the synthesized product. On the contrary, it may suggest that Cu ions are uniformly dispersed within anatase crystallites in the form of small clusters, therefore, diffraction originating from TiO_2 surface is more intense as compared to diffracted rays from Cu oxide. As a result, the intensity ratio of dopant peak is lower in comparison with the host material.[47,54,55] Fig. 5a depicts higher peak intensity of doped samples compared to control sample which signifies effective incorporation of Cu such that the dopant boosts the crystallinity and enhances the structural quality of host sample.[54] In addition, in Fig. 5a′ a notable shift of anatase reflection (101) to higher angles (25.3° to 25.9°) was observed with increasing dopant concentration. This may be caused by modification in anatase crystalline phase, since similarity in ionic radii of Cu^{2+} (0.72 Å) and Ti^{4+} (0.68 Å) is appropriate for interstitial incorporation of guest species into
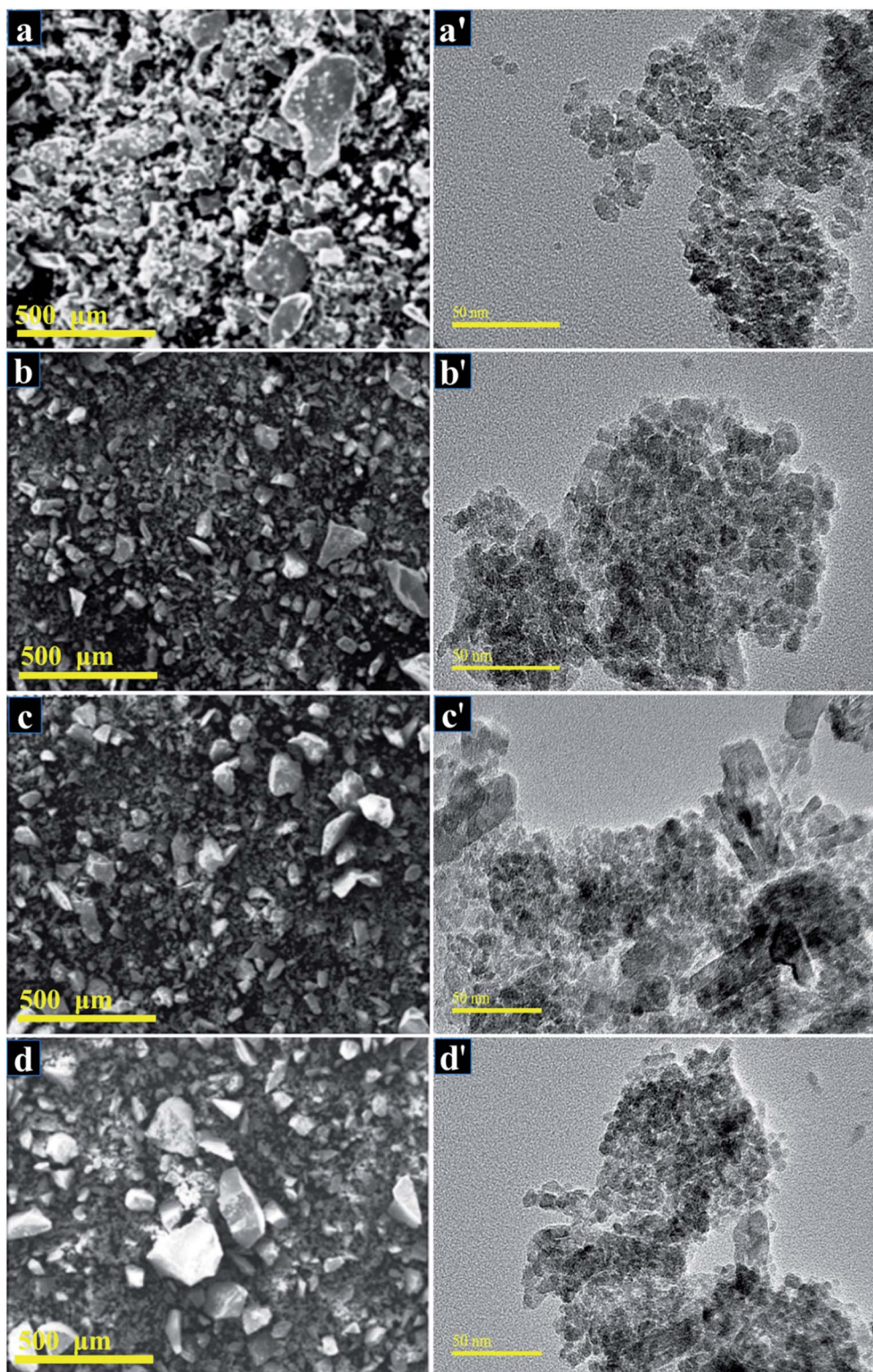
Fig. 8 (a–d) SEM images of 0 : 1, 0.03 : 1, 0.06 : 1, and 0.09 : 1 samples, respectively (a'–d') HR-TEM micrographs of TiO$_2$ and 0 : 03 : 1, 0.06 : 1, and 0.09 : 1 samples, respectively.

titania lattice.[47,56] The Cu^{2+} ions are placed among Ti^{4+} ions at interstitial sites owing to $r_{Ti} < r_{Cu}$, which produces a strain within titania lattice, therefore resulting in an upward shift of the peak (101).[56,57] The precise incorporation of Cu^{2+} associated with lower oxidation states in TiO$_2$ host lattice produces a charge-correct ion vacancy and decreases electron
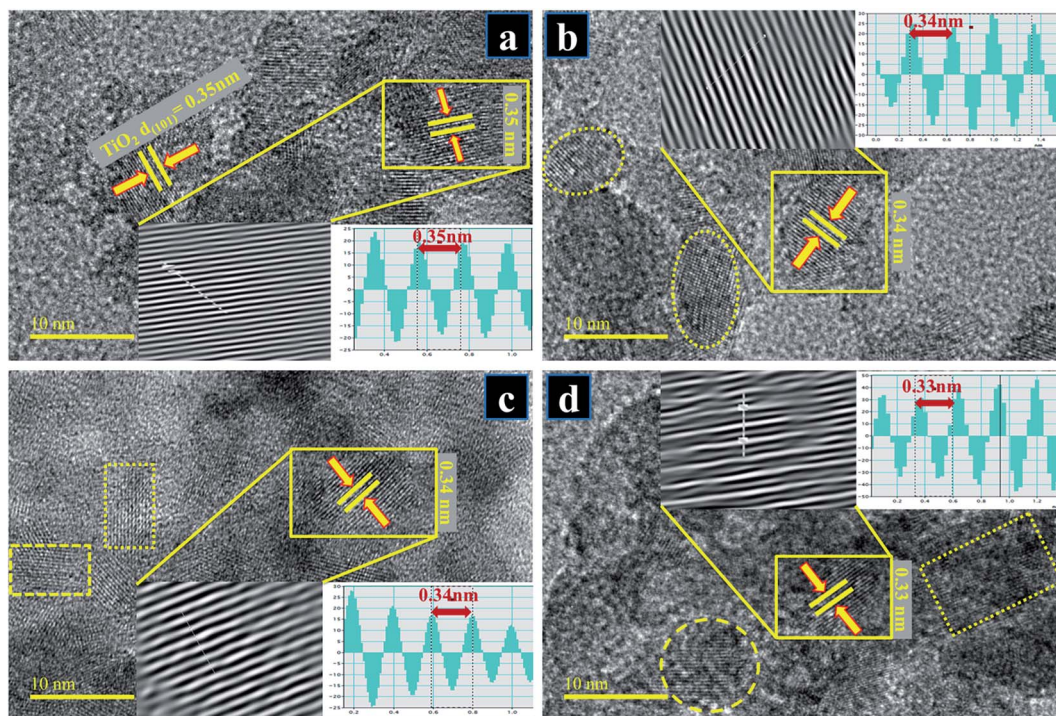
Fig. 9 (a–d) d-Spacings calculated from HR-TEM images obtained from Cu-TiO$_2$ (a) 0 : 1 (b) 0.03 : 1 (c) 0.06 : 1 (d) 0.09 : 1 samples.

concentration.[48] Furthermore, addition of Cu causes compressive stress, while a large number of dislocations are introduced when Cu ions are dispersed at interstitial sites within Ti lattice.

A decrease in crystallite size occurs with increasing dopant proportions as calculated by the Debye–Scherer equation (eqn (10)).[47,55,57–59]

Fig. 10 (a) PL spectra (b–d) EDS profiles of prepared samples (b) 0.03 : 1 (c) 0.06 : 1 (d) 0.09 : 1.

Fig. 11 (a–d): XRF data of Cu-doped TiO_2 (a) 0 : 1 (b) 0.03 : 1 (c) 0.06 : 1 (d) 0.09 : 1 samples.

$$D = \frac{0.9\lambda}{\beta \cos\theta} \tag{10}$$
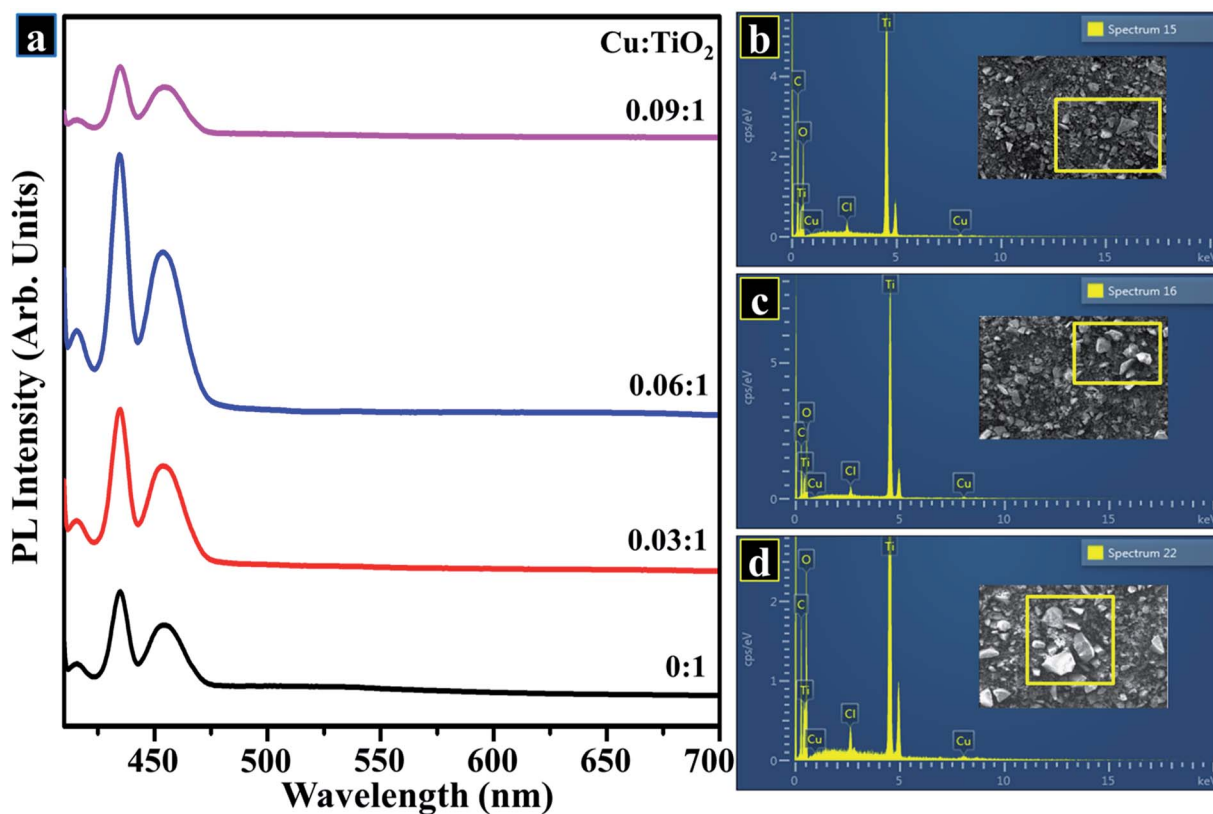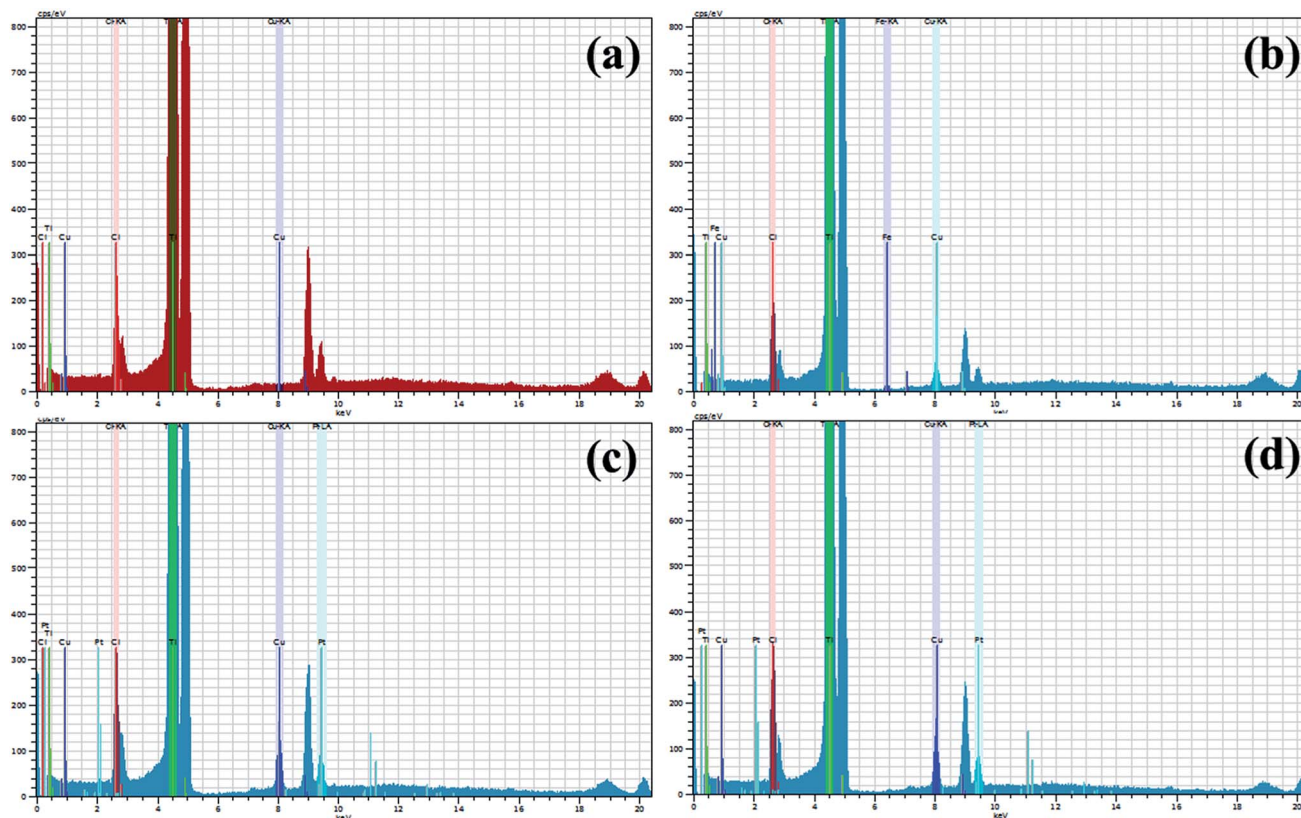
where D is the desired crystallite size and λ is wavelength of the radiation (0154 nm), β is full width at half maxima (FWHM) of the more intense peak (101). Calculated crystallite sizes are displayed in Table 1. SAED patterns of primeval sample and doped products display bright and discrete rings parallel to various planes of anatase phase of Cu-TiO_2 as revealed in Fig. 5b–e. These results are credited to well-crystallized samples and match well with XRD data.

Fig. 5f portrays IR spectra of pure and doped samples. It can be seen in the acquired spectrum that a sizeable absorption band is present between 400–1000 cm^{-1} that is ascribed to the vibration modes of Ti–O–Ti linkage in TiO_2 nanoparticles which signifies the formation of TiO_2.[59,60] The small absorption band around 1062 cm^{-1} in doped sample arises due to bonding of Ti–O–N.[60] Observed band between 3300–3600 cm^{-1} relates to stretching vibrations of hydroxyl group (O–H) and distinct band around 1632 cm^{-1} is attributed to the bending vibrations of hydroxyl ions (–OH). This vibration band is associated with the protons of physisorbed water in prepared samples.[59,61] According to the literature, titanium oxide preserves adsorbed undissociated water molecules owing to strong Lewis acidity of coordinatively unsaturated Ti^{4+} surface sites.[59]

UV-vis spectroscopy was used to study optical properties of prepared samples in terms of maximum absorption of ultra-visible light, band shift, and determination of band gap energy, as shown in the spectra displayed (200–700 nm) in Fig. 6a. Optical electronic excitations to conduction band from valence band are commonly depicted by enhancement of absorbance band with a certain wavelength in obtained absorption spectrum.[59] In acquired spectra, pristine TiO_2 exhibits absorption band around 310 nm, and Cu-doped samples also show this UV absorption band along with absorption tail trailing towards visible region (redshift).[48,55,59,62,63] The slight shift in absorption band up to 400 nm is caused by charge transfer from O 2p to Cu d-states. At maximum Cu concentration (sample 0.09 : 1), another broad band appears between 550–700 nm which is due to d–d electronic transitions of Cu^{2+} ion that possesses $3d^9$ electronic configuration with one electron in d-orbital.[62] Band gap energies were evaluated by using Tauc equation as described in eqn (11)

$$\alpha h\nu = K(h\nu - E_g)^n \tag{11}$$

where α is absorption coefficient, h denotes Planck's constant, ν is frequency and K is absorption index. The value of exponent (n) is associated with electronic nature of band gap and corresponds to direct allowed transitions (1/2), indirect allowed transitions (2), direct forbidden transitions (3/2), and indirect forbidden transitions (3).[64,65]

Fig. 6b–e depicts calculated band gap energies. Pure TiO_2, shown in Fig. 6b, exhibits a band gap energy of 3.1 eV while respective energies of Cu-doped samples (Fig. 6c–e) are listed in Table 1. It can be seen that the energy decreases with an
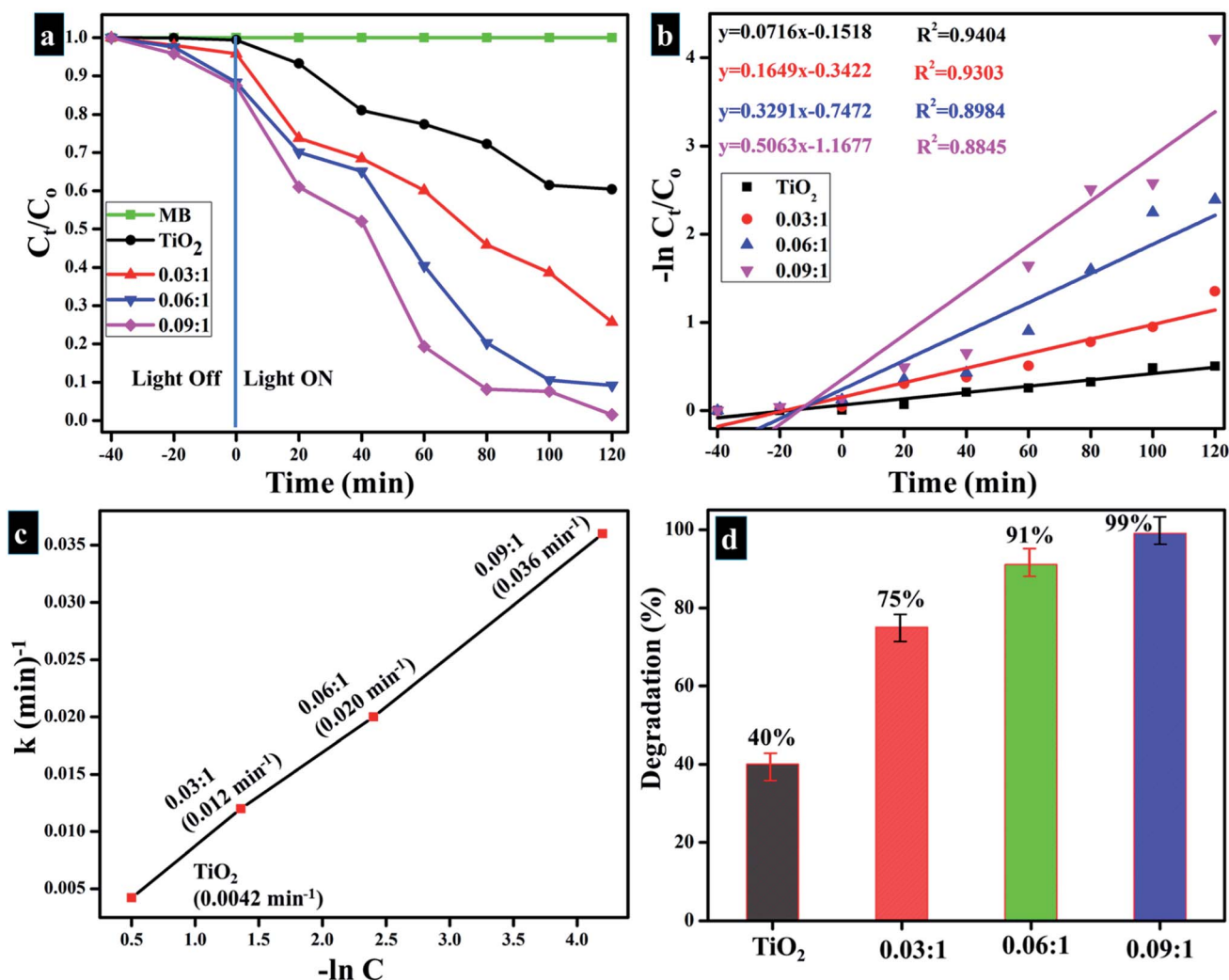
Fig. 12 (a) Plot of concentration ratio (C_t/C_o) versus time (b) plot of $-\ln(C_t/C_o)$ versus time spectra for dye reduction (c) rate constants of all samples (d) degradation (%) comparison of all samples.

increase in dopant concentration which is well corroborated by reported literature.[48,59,66] Doping with a transition metal such as Cu can induce new electronic phases in actual band gap which suggests that e$^-$ are excited by defect state of TiO_2 conduction band with less photon energy.[59] Drop in band gap energy with an increase in Cu concentration is attributed to Cu^{2+} ions that intercalated between host lattices of TiO_2 and generated oxygen vacancies due to charge compensation effect. In addition, band

Table 2   Comparative study of prepared sample with previously published data

| Cu-TiO$_2$ NPs							
Literature				Present study			
Synthesis	Phase	Max. degradation		Synthesis	Phase	Max. degradation	
Hydrothermal[22]	Anatase	90%	100 min	Sol–gel	Anatase	99%	120 min
Sol–gel[73]	Anatase	99%	180 min				
Sol–gel[5]	Anatase	98%	120 min				
Hydrothermal[47]	Anatase	90%	180 min				
Microwave-assisted sol–gel[11]	Anatase	90%	350 min				
Solvothermal[74]	Anatase	70%	120 min				
Sol–gel[55]	Anatase	99%	200 min				
Sol–gel[66]	Anatase	90%	180 min				
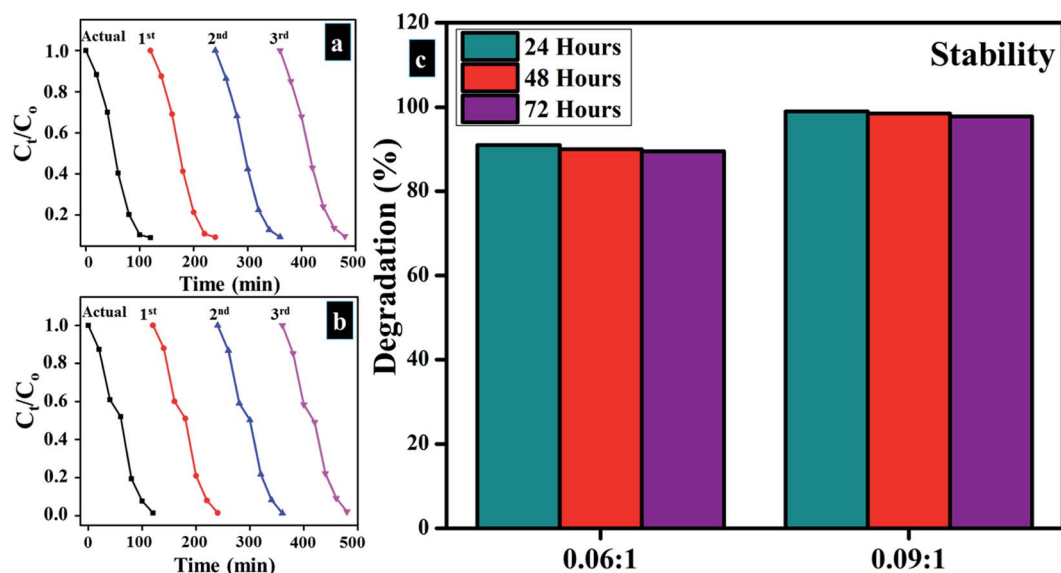
Fig. 13 (a and b) Plots of C_t/C_o vs. time for reusability of 0.06 : 1, and 0.09 : 1, respectively (c) stability of Cu-doped samples.

gap energy is reduced since Cu generates several new doping sites near the valance band of TiO_2 and therefore enriches visible absorption range by Cu 3d–Ti 3d optical transition.[47,48,59]

Fig. 7 is a schematic representation of the decrease in band gap energy of doped TiO_2 compared to host material. Fermi energy levels become close to valance band and conduction band resulting in a significant reduction in band gap (3.1–2.4 eV) of the prepared product.

SEM analysis was undertaken to observe the morphology and microstructure of Cu-doped TiO_2 as displayed in Fig. 8a–d. SEM images of composite show that all samples were polycrystalline and highly agglomerated. The agglomerations of doped samples seemed to be excessive compared to pure TiO_2.[67] Samples were further characterized using HRTEM analysis in order to elucidate the morphology and crystal structure as presented in Fig. 8a′–d′. HR-TEM micrographs show that Cu-
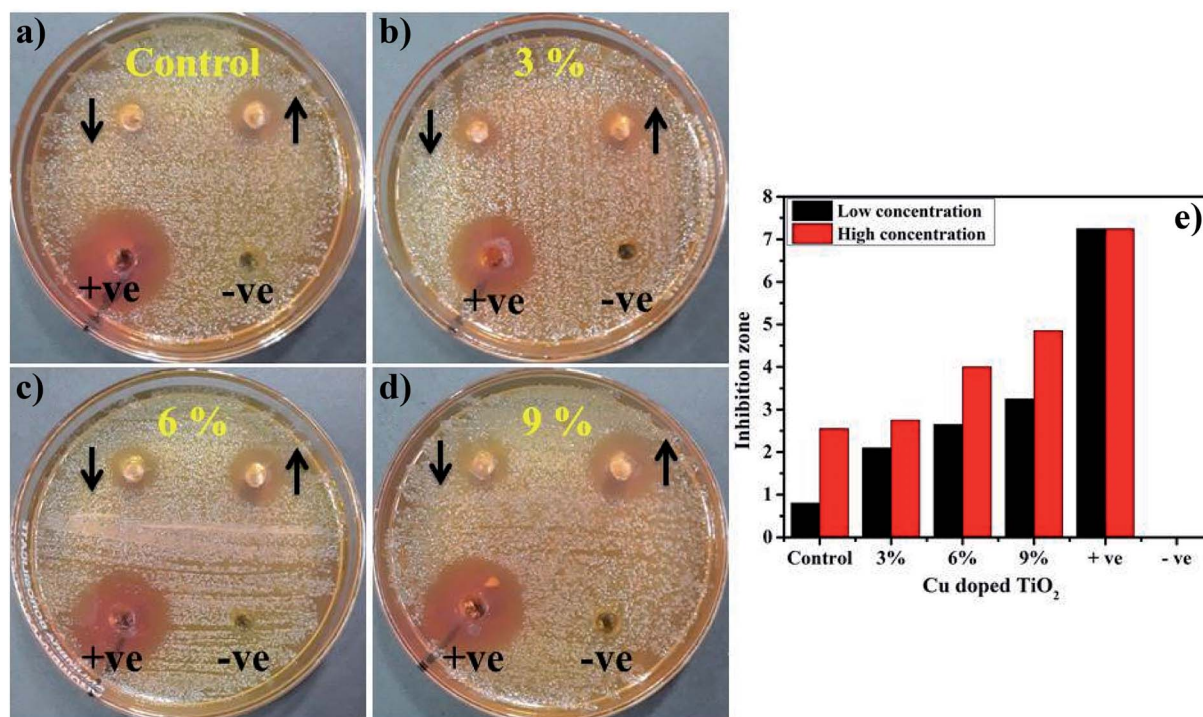

Fig. 14 (a–d) for S. aureus of all samples, name as mentioned in figure, respectively (e) graphical demonstration.

doped TiO_2 particles were spherical in nature and were uniformly distributed. It is reported in the literature that pure copper appears extremely dark rather black, however, it changes to greyish color when copper is deposited on TiO_2 particles.[68]

HR-TEM study at edge areas is a general and direct way to estimate the number of layers microscopically. HR-TEM micrographs shown in Fig. 9a–d on a single grain portray distinct atomic planes well-ordered in O–Ti–O arrangement to form a single layer and periodic atomic arrangement at particular areas, where interplanar spacing was measured to be ∼0.35 nm (Fig. 9a and b). According to the periodic arrangement in lattice fringe image, this matches up with (101) facet of anatase TiO_2 phase and corresponds well with XRD results.[52,53] In Fig. 9b–d with the addition of dopant, d-spacing of Cu-TiO_2 nanoparticles was found to be ∼0.34, 0.33 nm which is consistent with the peak shifts observed in XRD spectra (see Fig. 5a′).

Fig. 10a exhibits PL emission spectra of control and doped sample measured from 400 to 700 nm at room temperature with an exciting wavelength of 400 nm. PL emission spectrum was utilized to find out the efficacy of trapping as well as migration of charge carriers and to analyze the status of electron–hole-pairs. Since PL data is directly related to surface states, as a result, oxygen sites and defects are created on TiO_2 surface.[69] As shown in Fig. 10a, PL emission spectrum was detected with measurable intensities for undoped and Cu-doped TiO_2 in the range of 400–600 nm. These peaks perceived in the wavelength ranging from 400 to 600 nm are attributed to excitonic PL and an intense peak positioned at 431 nm indicates the presence of surface oxygen vacancies and defects on the TiO_2 sample surface.[70] With increasing concentration of Cu^{2+}, reduction in PL intensity was detected which can be ascribed to minor recombination rate of excitons suggesting an increase in separation efficiency. This could be associated with the electron-transfer process from conduction band (CB) which is the higher state of electrons to the new state incorporated by metal dopants. As reported earlier, emission spectrum positioned at 431 nm is considered a part of luminescent centers, which serves to enhance the photo-stability of TiO_2.[60,71] Tracing of elemental composition was achieved by means of EDS to assess purity of samples. According to the EDS profiles shown in Fig. 10b–d, strong peaks of Ti element at 0.9 and 4.9 keV, oxygen peak at 1.1 keV, Cu peaks at 1 and 5.6 keV were detected, which confirms the formation of pure anatase TiO_2 as well as suggests the successful incorporation of dopant species. A minor signal of Cl appearing in EDS spectra may be considered to be a small impurity picked up during sample preparation. Moreover, carbon peak appearing below 1 keV is caused by carbon tabs that are utilized to hold sample during SEM analysis or/and due to background counts in SEM-EDS detector.

X-ray fluorescence (XRF) technique was employed to further investigate the elemental/chemical composition of as-prepared product and to confirm the incorporation of dopant in the host sample as exhibited in Fig. 11, where Ti, Cu, Pt, Cl, and Fe were detected. The extracted data gives two main peaks of Ti and Cu at 0.4 keV and 8 keV, respectively which provides evidence for the presence of Ti and Cu in the synthesized sample.

Fig. 12a–d describes light-induced activity of Cu-doped TiO_2 nanoparticles. According to these findings, absorbance is presented as time-dependent function. Fig. 12a reveals photocatalytic response of nanoparticles and clearly shows that MB degradation gradually increases with increasing concentration of the dopant. Significant degradation is shown by the maximum doped sample (0.09 : 1) which was up to 99% in 120 minutes. Lesser extent of degradation was shown by samples in the dark whereas in the presence of light, considerable removal of MB was observed within 120 minutes. Only 40% degradation occurred in case of pure TiO_2, however with Cu incorporation, photocatalysts showed remarkable degradation since Cu reduces band gap and inhibits recombination rate. Fig. 12c shows rate constants of all samples calculated using pseudo-first-order kinetic theory:

$$-\ln(C_t/C_o) = kt$$

where k is the apparent rate constant that can be calculated and C (x-axis) represents ratio of C_t/C_o (Fig. 12c) as followed by the order 0.0042, 0.012, 0.020, and 0.036 min^{-1} for pure, 0.03 : 1, 0.06 : 1, and 0.09 : 1 samples, respectively. Fig. 12d shows % of degradation, maximum doped sample showed 99% degradation in a specific time. Cu-doped TiO_2 showed significant results when compared with the data reported in the literature and included in Table 2.[72,73] Based on these findings, Cu-doped TiO_2 can be considered to possess an excellent potential for use toward treatment of polluted water.

Table 3 Bactericidal action of Cu doped TiO_2

Sample	Inhibition zone[a] (mm)		Inhibition zone[b] (mm)	
	0.5 mg/50 μl	1.0 mg/50 μl	0.5 mg/50 μl	1.0 mg/50 μl
TiO_2	0	0	0.8	2.55
Cu-TiO_2 3.0%	0	0	2.1	2.75
Cu-TiO_2 6.0%	0	0	2.65	4
Cu-TiO_2 9.0%	0	0	3.25	4.85
Ciprofloxacin	4.25	4.25	7.25	7.25
DIW	0	0	0	0

[a] Inhibition zone (mm) of Cu doped TiO_2 for E. coli. [b] Inhibition zone measurements of Cu doped TiO_2 for S. aureus.

3.1 pH value

Treatments related to water purification depend highly upon pH values of the reaction solution. Extent of degradation of toxic dyes is mainly influenced by pH values as these are governed by a direct correlation. In the current study, photocatalysis mechanism was used to degrade MB under solar irradiation which also depends upon pH value. A literature survey shows that dye degradation can be successfully achieved under basic conditions. In this experiment, pH value was measured to be 8.9 which favorably supports the finding of the literature.

3.2 Stability

Stability is an important factor to consider while using a photocatalyst for water treatment. Generally, catalyst should be stable for a long time in order to achieve outstanding results. In the present study, the stability of photocatalyst was examined by allowing the performed activity to be retained for a minimum of three days. After every 24 hours, degradation of dye was inspected spectrophotometrically. Extracted results for 0.06 : 1 and 0.09 : 1 samples are displayed in the form of percentage degradation which was determined by means of eqn (a). Results displayed in Fig. 13c demonstrate outstanding stability of photocatalyst.

3.3 Reusability

The reusability of photocatalyst for numerous cycles is highly desirable in water treatment techniques. In this study,

reusability was investigated by recycling of 6 and 9 wt% doped photocatalyst up to three cycles, and the results were compared with the actual performance of the catalyst. As shown in Fig. 13a and b photocatalysts show promising results under recycling activity, which upholds outstanding reusability potential. Reusability results were also extracted spectrophotometrically.

3.4 Load of photocatalyst

Load of a photocatalyst also possesses abundant significance when dye degradation is tested for more than one cycle. In the present study, load of photocatalyst in an actually performed experiment (before) and after three cycles of recycling was measured. Minor weight loss was detected for photocatalyst ranges from 10 mg before and 9.5 mg after three cycles considering 5% sensing deviation.

The *in vitro* antimicrobial potential of Cu-doped TiO_2 against G −ve and G +ve isolates from ovine mastitic milk with graphical representations are shown in Fig. 14a–e and Table 3. The results depict enhanced bactericidal action and synergism of Cu-doped TiO_2 against *S. aureus* compared with *E. coli*, see Fig. 14a–e. Inhibition zones were recorded as (0.8–3.25 mm) and (2.55–4.85 mm) against *S. aureus* at low and high doses, respectively were found statistically significant ($P < 0.05$) while, all concentrations showed null efficacy against *E. coli* at a low and high dose. The % age efficacy increased from (11–44.8%) and (35.1–66.8%) against *S. aureus*. Ciprofloxacin as positive control inhibited (7.25 mm) and (4.25 mm) *S. aureus* and *E. coli* growth, respectively compared with DIW (0 mm). Overall Cu-doped TiO_2 showed null efficacy against G −ve bacteria while
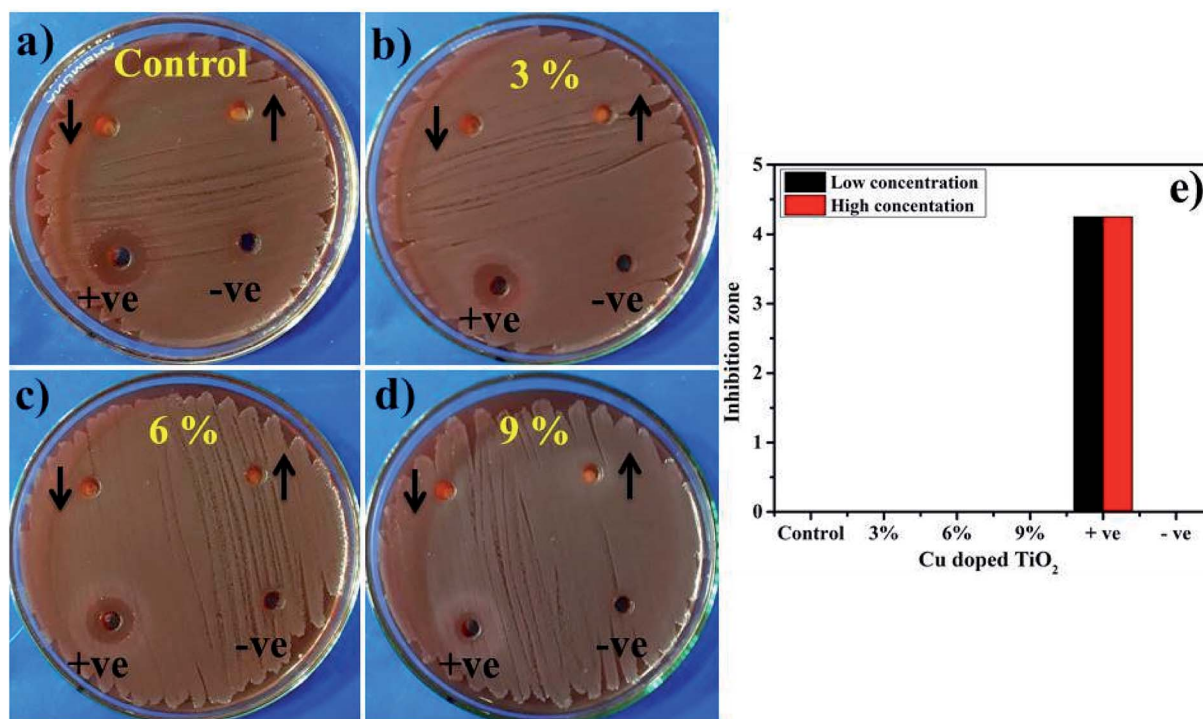

Fig. 15   (a) *In vitro* antimicrobial efficacy of TiO_2 (control), (b) 3% Cu-doped TiO_2 (c) 6% Cu-doped TiO_2, (d) 9% Cu-doped TiO_2 for *E. coli* (e) graphical presentation.
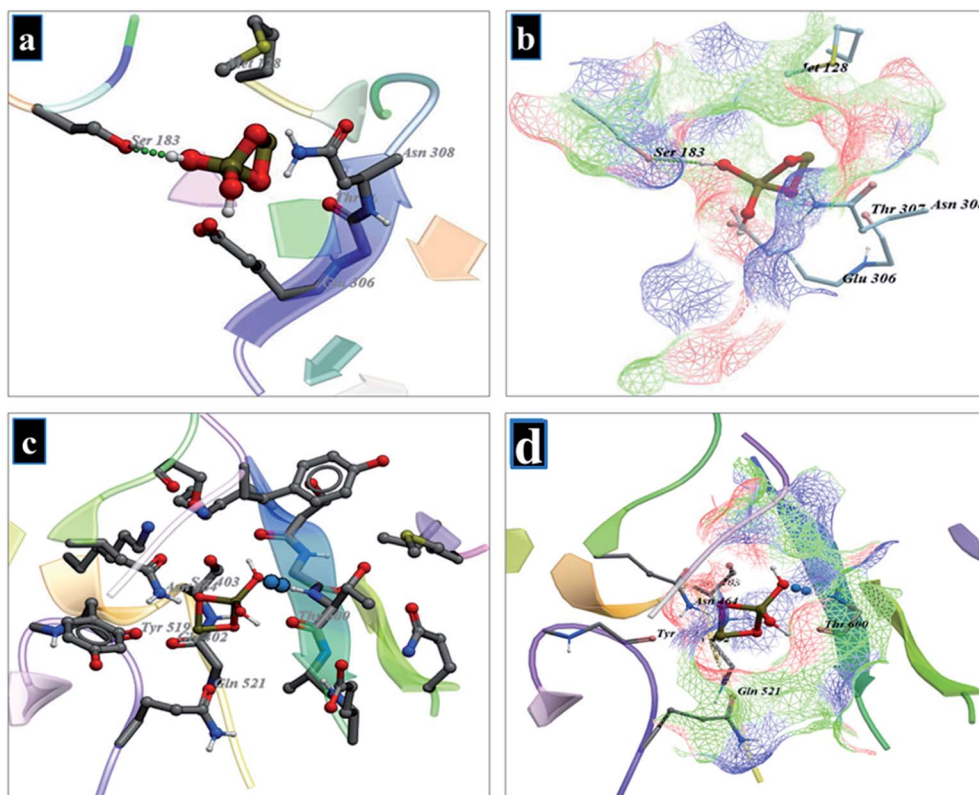
Fig. 16 (a and b) Binding interaction pattern of Cu–doped TiO$_2$ nanoparticle with active site residues of D–alanine-D-alanine ligase (ddlB), (c and d) β-lactamase from *S. aureus*.

doped material resulted in significant ($P < 0.05$) bactericidal efficacy against G +ve compared with G −ve (Fig. 14a–e).

The oxidative stress produced by nanoparticles directly depends on the concentration, shape, and size of NPs. Increase in antimicrobial presentation could be associated with more wt% doping of Cu-doped TiO$_2$ seen in terms of inhibition zones (mm) due to increased availability of cations. Antimicrobial effectiveness which depends on the concentration and size displays inverse relation to the size of doped material.[27,36,38,75] Small-sized NPs generate more reactive oxygen species (ROS) which halt effectively in implants of pathogenic bacteria membrane resulting in extrusion of cytoplasmic constituents thus killing bacteria[76,77] Secondly, the strong cationic interaction of Cu^{++} with negative parts of bacterial membrane results in significant bactericidal activity at high concentrations by inducing collapse and cell lysis of bacteria (Fig. 15).[19,31,38]

Molecular docking analysis of Cu-doped TiO$_2$ nanoparticles was performed to get an insight into mechanistic interactions with target enzymes. Enzymes involved in peptidoglycan synthesis represent well known, attractive, and viable targets for antibiotic discovery. Both D-alanine-D-alanine ligase (ddlB) and β-lactamase enzymes belong to biochemical machinery involved in peptidoglycan biosynthesis and their inhibition leads to cell wall rupture and ultimately death of bacteria. The binding energy obtained for best-docked conformation of Cu-doped TiO$_2$ nanoparticle into an active pocket of D-alanine-D-

alanine ligase (ddlB) was −5.67 kcal mol^{-1}. The Cu-doped TiO$_2$ interacted with Ser183 through H-bonding with a bond distance of 3.4 Å as shown in Fig. 16(a and b). Similarly, in case of β-lactamase, the binding score −4.91 kcal mol^{-1} is attributed to H-bonding interaction with Thr600 that has a bond distance of
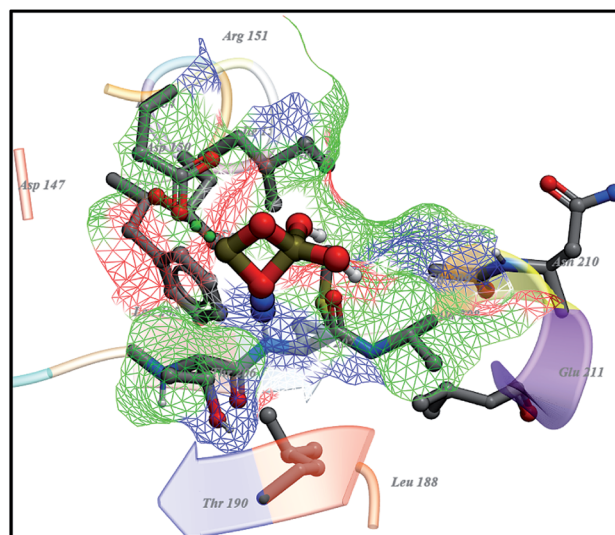

Fig. 17 Binding interaction pattern of Cu-doped TiO$_2$ nanoparticles with active site residues of enoyl-[acyl-carrier-protein] reductase (FabI) from *S. aureus*.

3.1 Å and metal-contact interaction with Gln521 as depicted in Fig. 16(c and d).

FabI has been validated as an excellent target for antibacterial drug development since it has been proven as a primary antibacterial target of the broad-spectrum antibiotics such as biocide, triclosan.[78] Therefore, specific inhibitors of FabI may be interesting lead compounds for developing effective antibacterial drugs. Molecular docking of Cu-doped TiO_2 nanoparticles into an active pocket of FabI showed H-bonding interaction with Met207 (bond distance: 2.8 Å) and Asp150 (bond distance: 2.2 Å) with docking score -6.13 kcal mol^{-1} as depicted in Fig. 17.

4 Conclusion

Cu-doped TiO_2 was successfully synthesized *via* sol–gel chemical method while prepared samples were analyzed through various characterization techniques. XRD profiles show the formation of anatase phase with a slight shift in (101) facet towards higher angle suggesting the presence of a dopant that is well dispersed in TiO_2 crystal. Crystallite size was reduced (22.22 to 15.47 nm) upon incorporation of Cu. All functional groups were related to the samples and characteristic absorption band between 400–1000 cm^{-1} was ascribed to the vibration modes of Ti–O–Ti linkage in TiO_2 nanoparticles that indicate the formation of pure TiO_2 as illustrated with FTIR. Spectrum obtained using UV-vis unveiled an absorption tail that trailed towards visible region (redshift) with increasing concentrations of dopant that caused the band gap to narrow (3.1 to 2.4 eV). Spherical morphology of nanoparticles exhibiting a high degree of agglomeration was visualized through SEM and HR-TEM with *d*-spacing of ~0.35 nm measured for pure sample and ~0.33 nm for sample doped with the highest concentration. A decrease in intensity of PL was credited to lower recombination rate of electron–hole pairs, which increases the separation efficiency. This may be associated with electron-transfer process from the conduction band that is the higher state of electrons to the new state incorporated by metal dopants. EDS and XRF spectra showed elemental composition that revealed successful doping of Cu. In addition, antimicrobial efficacy of Cu-doped TiO_2 against *S. aureus* and *E. coli* isolated directly from ovine mastitic milk resulted in significant quantitative values thereby, opening new horizons for doped nanomaterials use as potential antimicrobial agents. Owing to good binding scores and interaction patterns of Cu-doped TiO_2 nanoparticles with key amino acids of active sites unveiled by molecular docking study suggested them as potential inhibitors against β-lactamase, ddlB and FabI that could be further evaluated for its enzyme inhibition potential. Photocatalytic activity corresponding to Cu-TiO_2 (0.09 : 1) degraded 99% of MB concentration. These results obtained from formulated nanocatalysts demonstrate no hazardous behavior in wastewater treatment and point toward an excellent nanocatalyst that is stable, reusable and more importantly can be employed for the elimination of organic pollutants from wastewater. It can be regarded as a prospective nominee for possible antibacterial applications.

Availability of data

The data availability on request.

Conflicts of interest

The authors declare no conflict of interest.

Acknowledgements

References

1 A. Raza, M. Ikram, M. Aqeel, M. Imran, A. Ul-Hamid, K. N. Riaz and S. Ali, Enhanced industrial dye degradation using Co doped in chemically exfoliated MoS_2 nanosheets, *Appl. Nanosci.*, 2020, **10**, 1535–1544.

2 J. Moma and J. Baloyi, Modified Titanium Dioxide for Photocatalytic Applications, in *Photocatalysts - Applications and Attributes*, ed. S. Bahadar Khan and K. Akhtar, IntechOpen, 2019.

3 M. Sharma, K. Behl, S. Nigam and M. Joshi, TiO_2-GO nanocomposite for energy and environmental applications: a green synthesis approach, *Vacuum*, 2018, **156**, 434–439.

4 R. Katal, M. Salehi, M. H. Davood Abadi Farahani, S. Masudy-Panah, S. L. Ong and J. Hu, Preparation of a New Type of Black TiO_2 under a Vacuum Atmosphere for Sunlight Photocatalysis, *ACS Appl. Mater. Interfaces*, 2018, **10**, 35316–35326.

5 V. Kavitha, P. S. Ramesh and D. Geetha, Synthesis of Cu Loaded TiO_2 Nanoparticles for the Improved Photocatalytic Degradation of Rhodamine B, *Int. J. Nanosci.*, 2016, **15**, 1660002.

6 P. Ren, M. Song, J. Lee, J. Zheng, Z. Lu, M. Engelhard, X. Yang, X. Li, D. Kisailus and D. Li, Edge Dislocations Induce Improved Photocatalytic Efficiency of Colored TiO_2, *Adv. Mater. Interfaces*, 2019, **6**, 1901121.

7 A. M. Alotaibi, B. A. D. Williamson, S. Sathasivam, A. Kafizas, M. Alqahtani, C. Sotelo-Vazquez, J. Buckeridge, J. Wu, S. P. Nair, D. O. Scanlon and I. P. Parkin, Enhanced Photocatalytic and Antibacterial Ability of Cu doped Anatase TiO_2 Thin Films: Theory and Experiment, *ACS Appl. Mater. Interfaces*, 2020, **12**, 15348–15361.

8 K. Gupta, R. P. Singh, A. Pandey and A. Pandey, Photocatalytic antibacterial performance of TiO_2 and Ag-doped TiO_2 against S. aureus. P. aeruginosa and E. coli, *Beilstein J. Nanotechnol.*, 2013, **4**, 345–351.

9 M. Aqeel, S. Anjum, M. Imran, M. Ikram, H. Majeed, M. Naz, S. Ali and M. A. Ahmad, TiO_2 @ RGO (reduced graphene

oxide) doped nanoparticles demonstrated improved photocatalytic activity, *Mater. Res. Express*, 2019, **6**, 086215.

10 M. Janczarek and E. Kowalska, On the Origin of Enhanced Photocatalytic Activity of Copper-Modified Titania in the Oxidative Reaction Systems, *Catalysts*, 2017, **7**, 317.

11 S. M. Reda, M. Khairy and M. A. Mousa, Photocatalytic Activity of Nitrogen and Copper Doped TiO$_2$ Nanoparticles Prepared by Microwave-Assisted Sol-Gel Process, *Arabian J. Chem.*, 2020, **13**, 86–95.

12 M. Ikram, J. Hassan, M. Imran, J. Haider, A. Ul-Hamid, I. Shahzadi, M. Ikram, A. Raza, U. Qumar and S. Ali, 2D chemically exfoliated hexagonal boron nitride (hBN) nanosheets doped with Ni: synthesis, properties and catalytic application for the treatment of industrial wastewater, *Appl. Nanosci.*, 2020, DOI: 10.1007/s13204-020-01439-2.

13 M. Ikram, R. Tabassum, U. Qumar, S. Ali, A. Ul-Hamid, A. Haider, A. Raza, M. Imran and S. Ali, Promising performance of chemically exfoliated Zr-doped MoS$_2$ nanosheets for catalytic and antibacterial applications, *RSC Adv.*, 2020, **10**, 20559–20571.

14 M. Ikram, M. I. Khan, A. Raza, M. Imran, A. Ul-Hamid and S. Ali, Outstanding performance of silver decorated MoS$_2$ nanopetals used as nanocatalyst for synthetic dye degradation, *Phys. E*, 2020, **124**, 114246.

15 Q. Guo, C. Zhou, Z. Ma and X. Yang, Fundamentals of TiO$_2$ Photocatalysis: Concepts, Mechanisms, and Challenges, *Adv. Mater.*, 2019, **31**, 1901997.

16 A. Raza, U. Qumar, J. Hassan, M. Ikram, A. Ul-Hamid, J. Haider, M. Imran and S. Ali, A comparative study of dirac 2D materials, TMDCs and 2D insulators with regard to their structures and photocatalytic/sonophotocatalytic behavior, *Appl. Nanosci.*, 2020, DOI: 10.1007/s13204-020-01475-y.

17 S. Mathew, P. Ganguly, S. Rhatigan, V. Kumaravel, C. Byrne, S. Hinder, J. Bartlett, M. Nolan and S. Pillai, Cu-Doped TiO$_2$: Visible Light Assisted Photocatalytic Antimicrobial Activity, *Appl. Sci.*, 2018, **8**, 2067.

18 M. H. N. Assadi and D. A. H. Hanaor, The effects of copper doping on photocatalytic activity at (101) planes of anatase TiO$_2$: a theoretical study, *Appl. Surf. Sci.*, 2016, **387**, 682–689.

19 P. A. Charpentier, C. Chen, K. Azhie, B. Grohe, M. A. Mumin, A. F. Lotus, P. Therrien and S. Mittler, Photocatalytic and Antibacterial Activities of Silver and Iron Doped Titania Nanoparticles in Solution and Polyaspartic Coatings, *Nanotechnology*, 2019, **30**, 085706.

20 D. Rafieian, R. T. Driessen, W. Ogieglo and R. G. H. Lammertink, Intrinsic Photocatalytic Assessment of Reactively Sputtered TiO$_2$ Films, *ACS Appl. Mater. Interfaces*, 2015, **7**, 8727–8732.

21 J. Hassan, M. Ikram, A. Ul-Hamid, M. Imran, M. Aqeel and S. Ali, Application of Chemically Exfoliated Boron Nitride Nanosheets Doped with Co to Remove Organic Pollutants Rapidly from Textile Water, *Nanoscale Res. Lett.*, 2020, **15**, 75.

22 Y. Wang, W. Duan, B. Liu, X. Chen, F. Yang and J. Guo, The Effects of Doping Copper and Mesoporous Structure on Photocatalytic Properties of TiO$_2$, *J. Nanomater.*, 2014, **2014**, 1–7.

23 N. S. Leyland, J. Podporska-Carroll, J. Browne, S. J. Hinder, B. Quilty and S. C. Pillai, Highly Efficient F, Cu doped TiO$_2$ anti-bacterial visible light active photocatalytic coatings to combat hospital-acquired infections, *Sci. Rep.*, 2016, **6**, 24770.

24 B. Moongraksathum, J.-Y. Shang and Y.-W. Chen, Photocatalytic Antibacterial Effectiveness of Cu-Doped TiO$_2$ Thin Film Prepared via the Peroxo Sol-Gel Method, *Catalysts*, 2018, **8**, 352.

25 P.-C. Maness, S. Smolinski, D. M. Blake, Z. Huang, E. J. Wolfrum and W. A. Jacoby, Bactericidal Activity of Photocatalytic TiO$_2$ Reaction: toward an Understanding of Its Killing Mechanism, *Appl. Environ. Microbiol.*, 1999, **65**, 4094–4098.

26 L. Shen, Z. Xing, J. Zou, Z. Li, X. Wu, Y. Zhang, Q. Zhu, S. Yang and W. Zhou, Black TiO$_2$ Nanobelts/g-C$_3$N$_4$ Nanosheets Laminated Heterojunctions with Efficient Visible-Light-Driven Photocatalytic Performance, *Sci. Rep.*, 2017, **7**, 41978.

27 G. Cheng, Y. Wei, J. Xiong, Y. Gan, J. Zhu and F. Xu, Same titanium glycolate precursor but different products: successful synthesis of twinned anatase TiO$_2$ nanocrystal with excellent solar photocatalytic hydrogen evolution capability, *Inorg. Chem. Front.*, 2017, **4**, 1319–1329.

28 C. E. Santo, N. Taudte, D. H. Nies and G. Grass, Contribution of Copper Ion Resistance to Survival of Escherichia coli on Metallic Copper Surfaces, *Appl. Environ. Microbiol.*, 2008, **74**, 977–986.

29 M. Vincent, R. E. Duval, P. Hartemann and M. Engels-Deutsch, Contact killing and antimicrobial properties of copper, *J. Appl. Microbiol.*, 2018, **124**, 1032–1046.

30 C. E. Santo, E. W. Lam, C. G. Elowsky, D. Quaranta, D. W. Domaille, C. J. Chang and G. Grass, Bacterial Killing by Dry Metallic Copper Surfaces, *Appl. Environ. Microbiol.*, 2011, **77**, 794–802.

31 M. Ikram, S. Abbasi, A. Haider, S. Naz, A. Ul-Hamid, M. Imran, J. Haider and A. Ghaffar, Bi-metallic Ag/Cu incorporated into chemically exfoliated MoS$_2$ nanosheets to enhance antibacterial potential: insilico molecular docking studies, *Nanotechnology*, 2020, **31**, 275704.

32 M. Ikram, S. Ali, R. Murray, A. Hussain, Islah-u-din and S. I. Shah, Influence of fullerene derivative replacement with TiO$_2$ nanoparticles in organic bulk heterojunction solar cells, *Curr. Appl. Phys.*, 2015, **15**, 48–54.

33 S. Altaf, H. Ajaz, M. Imran, A. Ul-Hamid, M. Naz, M. Aqeel, A. Shahzadi, A. Shahbaz and M. Ikram, Synthesis and characterization of binary selenides of transition metals to investigate its photocatalytic, antimicrobial and anticancer efficacy, *Appl. Nanosci.*, 2020, DOI: 10.1007/s13204-020-01350-w.

34 A. Ajmal, I. Majeed, R. N. Malik, H. Idriss and M. A. Nadeem, Principles and mechanisms of photocatalytic dye degradation on TiO$_2$ based photocatalysts: a comparative overview, *RSC Adv.*, 2014, **4**, 37003–37026.

35 X. Pang, C. Chen, H. Ji, Y. Che, W. Ma and J. J. M. Zhao, Unraveling the photocatalytic mechanisms on TiO_2 surfaces using the oxygen-18 isotopic label technique, *Molecules*, 2014, **19**, 16291–16311.

36 A. Haider, M. Ijaz, M. Imran, M. Naz, H. Majeed, J. A. Khan, M. M. Ali and M. Ikram, Enhanced bactericidal action and dye degradation of spicy roots' extract-incorporated fine-tuned metal oxide nanoparticles, *Appl. Nanosci.*, 2020, **10**, 1095–1104.

37 U. L. N. H. Senarathna, S. S. N. Fernando, T. D. C. P. Gunasekara, M. M. Weerasekera, H. G. S. P. Hewageegana, N. D. H. Arachchi, H. D. Siriwardena and P. M. Jayaweera, Enhanced antibacterial activity of TiO_2 nanoparticle surface modified with Garcinia zeylanica extract, *Chem. Cent. J.*, 2017, **11**, 7.

38 A. Haider, M. Ijaz, S. Ali, J. Haider, M. Imran, H. Majeed, I. Shahzadi, M. M. Ali, J. A. Khan and M. Ikram, Green Synthesized Phytochemically (Zingiber officinale and Allium sativum) Reduced Nickel Oxide Nanoparticles Confirmed Bactericidal and Catalytic Potential, *Nanoscale Res. Lett.*, 2020, **15**, 50.

39 S. M. Drawz and R. A. Bonomo, Three Decades of-Lactamase Inhibitors, *Clin. Microbiol. Rev.*, 2010, **23**, 160–201.

40 B. A. Ellsworth, N. J. Tom and P. A. Bartlett, Synthesis and evaluation of inhibitors of bacterial D-alanine:d-alanine ligases, *Chem Biol.*, 1996, **3**, 37–44.

41 R. J. Heath and C. O. Rock, Enoyl-Acyl Carrier Protein Reductase (fabI) Plays a Determinant Role in Completing Cycles of Fatty Acid Elongation in Escherichia coli, *J. Biol. Chem.*, 1995, **270**, 26538–26542.

42 D. Lim and N. C. J. Strynadka, Enoyl-Acyl Carrier Protein Reductase (fabI) Plays a Determinant Role in Completing Cycles of Fatty Acid Elongation in Escherichia coli, *Nat. Struct. Biol.*, 2002, **9**, 870–876.

43 S. Liu, J. S. Chang, J. T. Herberg, M.-M. Horng, P. K. Tomich, A. H. Lin and K. R. Marotti, Allosteric inhibition of Staphylococcus aureus D-alanine:D-alanine ligase revealed by crystallographic studies, *Proc. Natl. Acad. Sci. U. S. A.*, 2006, **103**(41), 15178–15183.

44 D. C. McKinney, C. J. Eyermann, R.-F. Gu, J. Hu, S. L. Kazmirski, S. D. Lahiri, A. R. McKenzie, A. B. Shapiro and G. Breault, Antibacterial FabH Inhibitors with Mode of Action Validated in Haemophilus influenzae by in vitro Resistance Mutation Mapping, *ACS Infect. Dis.*, 2016, **2**, 456–464.

45 R. Abagyan and M. Totrov, Biased Probability Monte Carlo Conformational Searches and Electrostatic Calculations for Peptides and Proteins, *J. Mol. Biol.*, 1994, **235**, 983–1002.

46 A. Iftikhar, M. S. Khan, U. Rashid, Q. Mahmood, H. Zafar, M. Bilal and N. Riaz, Influence of metallic species for efficient photocatalytic water disinfection: bactericidal mechanism of in vitro results using docking simulation, *Environ. Sci. Pollut. Res.*, 2020, DOI: 10.1007/s11356-020-08974-z.

47 T. Aguilar, J. Navas, R. Alcántara, C. Fernández-Lorenzo, J. J. Gallardo, G. Blanco and J. Martín-Calleja, A route for the synthesis of Cu-doped TiO_2 nanoparticles with a very low band gap, *Chem. Phys. Lett.*, 2013, **571**, 49–53.

48 R. Kamble, S. Mahajan, V. Puri, H. Shinde and K. Garadkar, Visible Light-Driven high Photocatalytic Activity of Cu-Doped TiO_2 Nanoparticles Synthesized by Hydrothermal Method, *Mater. Sci. Res. India*, 2018, **15**, 197–208.

49 X. Wei, G. Zhu, J. Fang and J. Chen, Synthesis, Characterization, and Photocatalysis of Well-Dispersible Phase-Pure Anatase TiO_2 Nanoparticles, *Int. J. Photoenergy*, 2013, **2013**, 1–6.

50 S. Phromma, T. Wutikhun, P. Kasamechonchung, T. Eksangsri and C. Sapcharoenkun, Effect of Calcination Temperature on Photocatalytic Activity of Synthesized TiO_2 Nanoparticles via Wet Ball Milling Sol-Gel Method, *Appl. Sci.*, 2020, **10**, 993.

51 Y. Zhang, Y. Meng, K. Zhu, H. Qiu, Y. Ju, Y. Gao, F. Du, B. Zou, G. Chen and Y. Wei, Copper-Doped Titanium Dioxide Bronze Nanowires with Superior High Rate Capability for Lithium Ion Batteries, *ACS Appl. Mater. Interfaces*, 2016, **8**, 7957–7965.

52 M. Xu, F. Teng, J. Xu, T. Lu and M. Chen, Etched titania nanoplates by both HF and HAc and the photocatalytic activities for degradation of pollutants, *RSC Adv.*, 2014, **4**, 8023.

53 S. Dai, Y. Wu, T. Sakai, Z. Du, H. Sakai and M. Abe, Preparation of Highly Crystalline TiO_2 Nanostructures by Acid-assisted Hydrothermal Treatment of Hexagonal-structured Nanocrystalline Titania/Cetyltrimethyammonium Bromide Nanoskeleton, *Nanoscale Res. Lett.*, 2010, **5**, 1829–1835.

54 A. A. Kashale, P. K. Dwivedi, B. R. Sathe, M. V. Shelke, J.-Y. Chang and A. V. Ghule, Biomass-Mediated Synthesis of Cu-Doped TiO_2 Nanoparticles for Improved-Performance Lithium-Ion Batteries, *ACS Omega*, 2018, **3**, 13676–13684.

55 V. Rajendran, G. Rajendran and N. Karuppathevar, Phtotocatalytic Degradation of Methyelene Blue by Cu Doped TiO_2 Thin Films under Visible Light Irradiation, *Mechanics, Materials Science & Engineering*, 2017, **7**, DOI: 10.2412/mmse.81.84.608.

56 R. López, R. Gómez and M. E. Llanos, Photophysical and photocatalytic properties of nanosized copper-doped titania sol–gel catalysts, *Catal. Today*, 2009, **148**, 103–108.

57 M. Sahu and P. Biswas, Single-step processing of copper-doped titania nanomaterials in a flame aerosol reactor, *Nanoscale Res. Lett.*, 2011, **6**, 441.

58 T. Wang, X. Meng, G. Liu, K. Chang, P. Li, Q. Kang, L. Liu, M. Li, S. Ouyang and J. Ye, In situ synthesis of ordered mesoporous Co-doped TiO_2 and its enhanced photocatalytic activity and selectivity for the reduction of CO_2, *J. Mater. Chem. A*, 2015, **3**, 9491–9501.

59 R. J. Alvaro, N. D. Diana and A. M. Maria, Effect of Cu on Optical Properties of TiO_2 Nanoparticles, *Contemp. Eng. Sci.*, 2017, **10**, 1539–1549.

60 B. Rajamannan, S. Mugundan, G. Viruthagiri, P. Praveen and N. Shanmugam, Linear and nonlinear optical studies of bare and copper doped TiO_2 nanoparticles via sol gel technique, *Spectrochim. Acta, Part A*, 2014, **118**, 651–656.

61 Z. A. Ansari, A. Umar, H. Fouad and S. G. Ansari, Dye Sensitized Solar Cells Fabricated Using Cu-Doped TiO_2

Nanopowder with Anthocyanin as Sensitizer, *J. Nanoelectron. Optoelectron.*, 2015, **10**, 290–294.

62 B. Choudhury, M. Dey and A. Choudhury, Shallow and deep trap emission and luminescence quenching of TiO_2 nanoparticles on Cu doping, *Appl. Nanosci.*, 2014, **4**, 499–506.

63 O. Ola and M. Mercedes Maroto-Valer, Copper based TiO_2 honeycomb monoliths for CO_2 photoreduction, *Catal. Sci. Technol.*, 2014, **4**, 1631–1637.

64 S. K. Suram, P. F. Newhouse and J. M. Gregoire, High Throughput Light Absorber Discovery, Part 1: An Algorithm for Automated Tauc Analysis, *ACS Comb. Sci.*, 2016, **18**, 673–681.

65 R. S. Vemuri, M. H. Engelhard and C. V. Ramana, Correlation between Surface Chemistry, Density, and Band Gap in Nanocrystalline WO_3 Thin Films, *ACS Appl. Mater. Interfaces*, 2012, **4**, 1371–1377.

66 K. Vijayalakshmi and D. Sivaraj, Synergistic antibacterial activity of barium doped TiO_2 nanoclusters synthesized by microwave processing, *RSC Adv.*, 2016, **6**, 9663–9671.

67 M. Hamadanian, S. Karimzadeh, V. Jabbari and D. Villagrán, Synthesis of cysteine, cobalt and copper-doped TiO_2 nanophotocatalysts with excellent visible-light-induced photocatalytic activity, *Mater. Sci. Semicond. Process.*, 2016, **41**, 168–176.

68 A. Teleki, N. Bjelobrk and S. Pratsinis, Flame-made Nb- and Cu-doped TiO_2 sensors for CO and ethanol, *Sens. Actuators, B*, 2008, **130**, 449–457.

69 G. J. Thangama, J. J. Devadasana and P. S. Gracea, Cu Doped TiO_2 Thin Films Fabricated by Simple SPD Technique, *IOSR J. Appl. Phys.*, 2017, **03**, 57–60.

70 H. M. Yadav, S. V. Otari, V. B. Koli, S. S. Mali, C. K. Hong, S. H. Pawar and S. D. Delekar, Preparation and characterization of copper-doped anatase TiO_2 nanoparticles with visible light photocatalytic antibacterial activity, *J. Photochem. Photobiol., A*, 2014, **280**, 32–38.

71 W. Zhang, Y. Liu, B. Yu, J. Zhang and W. Liang, Effects of silver substrates on the visible light photocatalytic activities of copper-doped titanium dioxide thin films, *Mater. Sci. Semicond. Process.*, 2015, **30**, 527–534.

72 Z. Yao, H. Sun, H. Sui and X. Liu, 2D/2D Heterojunction of R-scheme Ti_3C_2 MXene/MoS_2 Nanosheets for Enhanced Photocatalytic Performance, *Nanoscale Res. Lett.*, 2020, **15**(1), 78.

73 M. Ikram, A. Raza, M. Imran, A. Ul-Hamid, A. Shahbaz and S. Ali, Hydrothermal Synthesis of Silver Decorated Reduced Graphene Oxide (rGO) Nanoflakes with Effective Photocatalytic Activity for Wastewater Treatment, *Nanoscale Res. Lett.*, 2020, **15**, 95.

74 I. Ganesh, P. P. Kumar, I. Annapoorna, J. M. Sumliner, M. Ramakrishna, N. Y. Hebalkar, G. Padmanabham and G. Sundararajan, Preparation and characterization of Cu-doped TiO_2 materials for electrochemical, photoelectrochemical, and photocatalytic applications, *Appl. Surf. Sci.*, 2014, **293**, 229–247.

75 H. Liu, M. Zou, B. Viliam Hakala, R. Sefiu Abolaji and M. Yang, Synthesis, characterization of Cu, N co-doped TiO_2 microspheres with enhanced photocatalytic activities, *Adv. Mater. Sci.*, 2017, **2**(1), 1–7, DOI: 10.15761/AMS.1000114.

76 U. Qumar, M. Ikram, M. Imran, A. Haider, A. Ul-Hamid, J. Haider, K. N. Riaz and S. Ali, Synergistic effect of Bi-doped exfoliated MoS_2 nanosheets on their bactericidal and dye degradation potential, *Dalton Trans.*, 2020, **49**, 5362–5377.

77 W. Fang, C. X. Chaofa Xu, J. Zheng, G. Chen and K. Jiang, Fabrication of Cu–Ag bimetal nanotube-based copper silicates for enhancement of antibacterial activities, *RSC Adv.*, 2015, **5**, 39612–39619.

78 R. J. Heath, J. R. Rubin, D. R. Holland, E. Zhang, M. E. Snow and C. O. Rock, Mechanism of Triclosan Inhibition of Bacterial Fatty Acid Synthesis, *J. Biol. Chem.*, 1999, **274**, 11110–11114.